Ore Geology Reviews 163 (2023) 105765

Contents lists available at ScienceDirect

Ore Geology Reviews

journal homepage: www.elsevier.com/locate/oregeorev

The ore genesis of the Shagou Ag-Pb-Zn deposit in the Southern North China Craton: Constraints from He-Ar-Pb isotopes and trace element compositions of sphalerite

Jinhong Xu [a,b,c], Yujia Zhang [d], Kaiwen Li [d], Chaofei Zheng [e], Xiyao Li [b,f], Ziru Jin [b,f], Chengquan Wu [b,f,*], Zhengwei Zhang [b,f,*]

[a] Institute of Resources and Environment, Tongren University, 554300, China
[b] State Key Laboratory of Ore Deposit Geochemistry, Institute of Geochemistry, Chinese Academy of Sciences, Guiyang 550018, China
[c] Institute of Fanjingshan National Park, Tongren 554300, China
[d] Henan Academy of Geology, Zhengzhou 450016, China
[e] Enterprise Alliance Service Center, Wuyi University, Jiangmen 529000, China
[f] University of Chinese Academy of Sciences, Beijing 100049, China

ARTICLE INFO

Keywords:
He-Ar-Pb isotope
Trace element
Vein Ag-Pb-Zn deposit
Shagou
Southern North China Craton

ABSTRACT

Shagou is one of the largest Ag-Pb-Zn deposits with the highest grade of Ag (Ag 1754 t @284 g/t Ag, locally up to 20,000 g/t) in the Southern North China Craton. Four mineralization stages have been identified, with assemblages of: (I) quartz + siderite + pyrite, (II) quartz + dark-brown sphalerite + fine galena + silver minerals, (III) quartz + ankerite + light-brown sphalerite + coarse galena + silver minerals, and (IV) quartz + calcite (IV). Silver minerals were mainly deposited during stage III, in which polybasite and freibergite were the dominant Ag-bearing ore minerals. He-Ar isotope compositions suggest that the ore-forming fluids of the Shagou deposit were derived from a mix of crustal and mantle sources. In situ Pb isotope comparison with regional strata, magmatic rocks, and sulfides from nearby ore deposits indicate that Pb and other metals (e.g., Ag and Zn) of the Shagou deposit originated from both the Mesozoic granite, the surrounding Taihua Group and the Meso-Neoproterozoic marine sediments. LA-ICP-MS analyses revealed that the Ag content of the dark-brown sphalerite was one order of magnitude higher than that of the light-brown sphalerite, suggesting that fluid cooling coupled with decreases in $\log fO_2$ and $\log fS_2$ were the major factors that promoting extensive Ag deposition. Dark-brown and light-brown sphalerites were enriched in In (up to 474 ppm), consistent with magmatic-related deposits. The newly obtained data in this study, combined with previous results, support a magmatic-hydrothermal origin for the Shagou Ag-Pb-Zn deposit.

1. Introduction

Vein-type silver-lead–zinc deposits have made important contributions of Ag and base metals; however, their genesis remains controversial (Beaudoin and Sangster, 1992; Kissin and Mango, 2014). Fluid inclusion, stable isotope, elemental geochemistry, and geochronological data suggest that some Ag-Pb-Zn vein mineralization has a close temporal, spatial, and genetic association with porphyry-type mineralization (Sillitoe, 2010; Bonsall et al., 2011; Li et al., 2017; Zhai et al., 2018, 2020; Jin et al., 2019). However, some Ag-Pb-Zn vein deposits are hosted within amphibolite-facies metamorphic rocks and are far from porphyry intrusions, and their genesis remains poorly understood (Beaudoin and Sangster, 1992; Li et al., 2013; Kissin and Mango, 2014).

The Xiayu, Nannihu, and Fudian ore fields of the Southern North China Craton (SNCC, Fig. 1) contain substantial Ag-Pb-Zn vein mineralization. This area is well-known for its mining history and has been the subject of research into polymetallic vein-type mineralization (Peng, 1994; Mao et al., 2006; Cao et al., 2015; Li et al., 2016). The hydrothermal veins in the Nannihu and Fudian ore fields have close temporal, spatial, and genetic associations with porphyry-type mineralization and are well documented (Cao et al., 2015; Li et al., 2017; Jin et al., 2019). Although extensive research has been conducted on such deposits in the Xiayu ore field, resulting in large amounts of stable isotope, geochronological, and fluid inclusion data (Sui et al., 2000; Chen et al., 2004;

* Corresponding authors at: State Key Laboratory of Ore Deposit Geochemistry, Institute of Geochemistry, Chinese Academy of Sciences, Guiyang 550018, China.
E-mail addresses: wuchengquan@mail.gyig.ac.cn (C. Wu), zhangzhengwei@mail.gyig.ac.cn (Z. Zhang).

https://doi.org/10.1016/j.oregeorev.2023.105765
Received 28 August 2023; Received in revised form 21 October 2023; Accepted 4 November 2023
Available online 10 November 2023

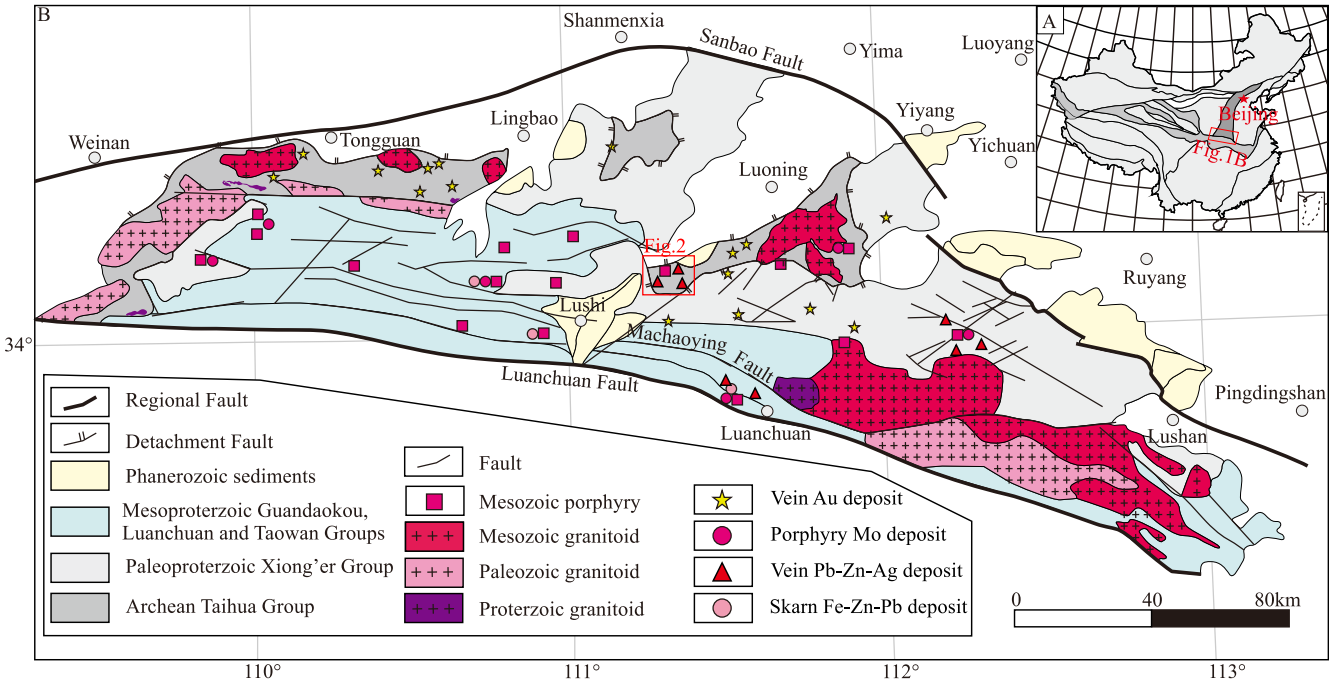

Figure 1

Fig. 1. A. Schematic map showing the tectonic units of China. B. Simplified geological map showing major mining districts in the Southern North China Craton (modified from Hu and Lin, 1988; Zhang et al., 2001).

Mao et al., 2006; Gao et al., 2011; Han et al., 2013, 2014; Li et al., 2013, Li et al., 2016), the mechanisms of ore formation and the ore genesis and nature of the involved fluids are not fully constrained.

The Shagou deposit is located in the west of the Xiayu ore field (Fig. 2) and contains more than 43 veins with a total resource of 6.77 Mt of ore containing 1,754 t Ag @ 284 g/t, 0.38 Mt Pb @ 5.60 wt% and 0.19 Mt Zn @ 2.82 wt% (Smith et al., 2020), making it the largest and richest silver deposit in the SNCC. Compared with similar deposits in this region, this deposit is particularly enriched in Ag, with grades of up to 20,000 g/t (Zheng et al., 2006; Stephenson et al., 2016). However, the genesis of these Ag-Pb-Zn veins remains controversial. C-O-S-H-Sr isotope data suggest that this deposit is linked to the metamorphic devolatilization of Proterozoic marine sediments and researchers have since classified it as an orogenic deposit (Han et al., 2013, Han et al., 2014) or a crustal-extension Ag-Pb-Zn mineralization (Li et al., 2013). In contrast, new geochronological and fluid inclusion data indicate that the Ag-Pb-Zn veins were formed during the Early Cretaceous, coeval with nearby magmatism-metallogenesis in the SNCC, as part of a magmatic-hydrothermal system (Mao et al., 2006, 2010; Gao et al., 2011; Tian et al., 2023).

We present comprehensive mineralogy, He-Ar-Pb isotope geochemistry, and trace element analyses of sphalerite to further constrain the ore-forming material source, mechanism, and genesis of the Shagou deposit.

2. Geological setting

The Xiayu ore field is located in the Xiong'ershan district of the SNCC (Fig. 1; Li et al., 1993; Dong et al., 2011). The westward subduction of the paleo-Pacific Plate during the Early Mesozoic triggered tectonic reactivation or lithospheric destruction of the North China Craton (Zhu et al., 2012). As a result, extensive magmatism-metallogenesis has occurred in the SNCC (Mao et al., 2010), along with exhumation of numerous metamorphic core complexes (Fig. 1; Shi et al., 2004) and the development of intracontinental rift basins (Ren et al., 2002).

The SNCC is dominated by the Late Archean to Early Paleoproterozoic basement of the Taihua Group and cover layers of Paleoproterozoic Xiong'er Group volcanic rocks (Fig. 1B; Hu et al., 1988; Zhang et al., 2003). The Taihua Group consists of medium- to high-grade metamorphic amphibolite, TTG gneiss, argillaceous gneiss, and fine-grained granite (Zhang et al., 1985); this group underwent 1.95 and 1.85 Ga amphibolite to granulite facies metamorphism (Li et al., 2015 and references therein). The Xiong'er Group volcanic rocks are dominated by andesite, and were erupted at 1.78, 1.76–1.75, and 1.65–1.45 Ga, with a major phase at 1.78 Ga (He et al., 2009; Zhao et al., 2004, Zhao and Zhou, 2009; Wang et al., 2010, Wang et al., 2019). The Xiong'er Group volcanic rocks are unconformably overlain by the 1.3–0.8 Ga Guandaokou, Luanchuan, and Taowan Groups (GLT Groups) to the south (Hu et al., 1988).

The Xiong'ershan district is characterized by the Xiong'ershan metamorphic core complex, with the Luoning detachment fault separating the lower Taihua Group and upper Xiong'er Group from the Mesozoic to Cenozoic terrestrial sedimentary rocks (Figs. 1-2; Shi et al., 2004). The EW-trending Machaoying Fault has been interpreted as a transcrustal structure based on geophysical data (Hu et al., 1988), and reactivated in the Early Cretaceous (Zhang et al., 2006; Han et al., 2009). Secondary higher-order faults are well distributed throughout the Xiong'ershan district and adjacent areas, and control the distribution of the Au-Ag-Pb-Zn-Mo deposits (Figs. 1 and 2). These structures were dominated by an early compressional regime which transformed into a late extensional fault (Mao et al., 2006; Gao et al., 2011).

Mesozoic granitoid intrusions are well distributed within the Xiong'ershan district and surrounding areas, and are characterized by the Huashan complex, several ore-bearing porphyries, and explosive breccias (Fig. 1). The Huashan granitoid complex is composed of Wuzhangshan, Haoping, and Jinshanmiao plutons. These three granitic batholiths have SHRIMP zircon U-Pb ages of 156.8 ± 1.2, 130.7 ± 1.4, and 130.7 ± 1.4 Ma, respectively (Li, 2005). The breccia pipes are mainly represented by Qiyugou Au-bearing breccia pipes (Wang et al., 2001; Ren et al., 2002). In addition, a series of Mo-mineralized porphyries were emplaced between the Late Jurassic and Early Cretaceous (Li, 2005; Mao et al., 2010). These Yanshanian granitoid intrusions and

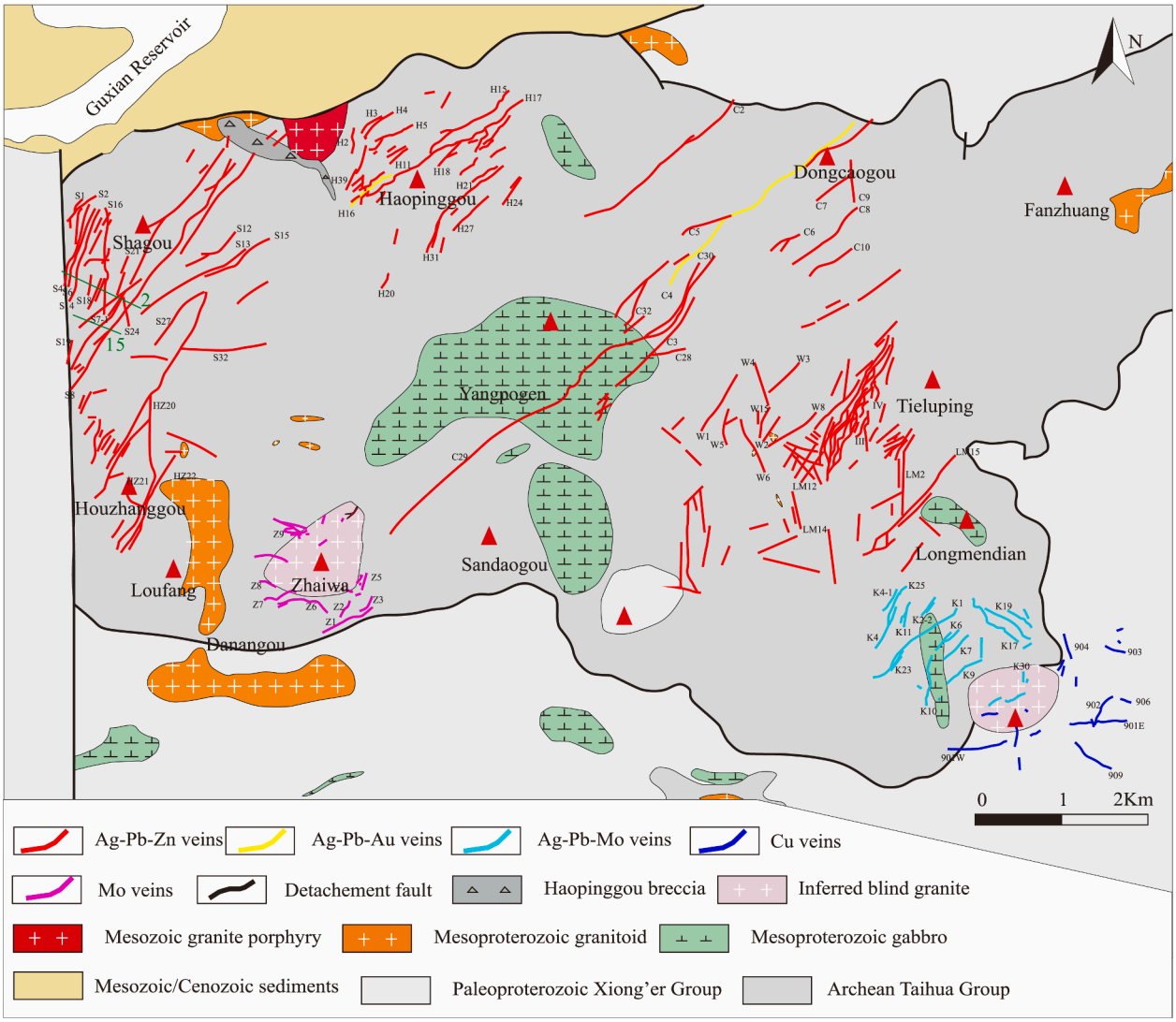

Fig. 2. Geological map showing distribution of ore veins for the Shagou Ag-Pb-Zn deposit in the Xiayu ore field (simplified from Mao et al., 2006; Stephenson et al., 2016; Smith et al., 2020). For location of the map see Fig. 1.

related hypabyssal intrusions are associated with Mesozoic extensional tectonics in the SNCC (Chen and Fu, 1992).

3. Deposit geology

The Xiayu ore field is endowed with numerous medium-to-large-scale Ag-Pb-Zn deposits and is the major Ag-Pb-Zn vein mineralization in the SNCC (Figs. 1-2). This ore field is located within the southern margin of the Xiong'ershan metamorphic core complex and is dominated by the Taihua and Xiong'er groups (Figs. 1 and 2; Shi et al., 2004). Mesozoic and Cenozoic sedimentary rocks are locally present in the mining area (Fig. 2).

High-angle NE- to NNE-striking extensional faults are widespread in the Xiayu ore field and control the distribution of the Ag-Pb-Zn veins (Fig. 2). Most of the faults dip to the northwest, with some dipping to the southeast. Widely-distributed mafic-to-felsic magma has intruded the Taihua Group in the mine field (Fig. 2). Zircon U-Pb ages reveal that these mafic intrusions emplaced during the Paleoproterozoic (Han et al., 2015). A few granite dikes occur in the southern and eastern areas of the mine and have LA-ICP-MS zircon U-Pb ages of 1805 ± 12 Ma and 1792 ± 14 Ma, respectively (Xu et al., 2021). Zhai'ao syenite granite dikes occur in the south, and have a SHRIMP zircon U-Pb age of 217.7 ± 3.6 Ma (Li et al., 2012). The Haopinggou porphyry is exposed in the north of the Xiayu ore field and consists of megacrystic granite porphyry (130–135 Ma; Ye, 2006; Guo et al., 2009; Mao et al., 2010; Liang et al., 2015; Tian et al., 2023) and granite porphyry (125.9 ± 0.7 Ma; Tian et al., 2023). Geophysical data suggest that concealed granites exist to the west and south of the mine (Fig. 2; Zhang and Zhu, 1996; Wang et al., 1997; Cao et al., 2017).

The Shagou Ag-Pb-Zn deposit is located in the northwestern part of the Xiayu Ore Field (Figs. 2 and 3). More than 43 hydrothermal alteration veins have been identified, all hosted within amphibolite facies metamorphic rocks of the Late Archean to Early Paleoproterozoic Taihua Group (Fig. 2; Stephenson et al., 2016). The geometric and chemical features of the major veins are summarized in Table 1. Most mineralization veins have NNE to NE strikes and dips of 60–95 to the NNW, vary in width from 0.7 to 10 m, and have been traced along strike for distances of 370 to 3,000 m. Vein S16 and S16E strike nearly N-S (Fig. 3). These mineralization veins are characterized by extensional shear features and have 2–8 ore orebodies which range from 25 to 215 m long, and 0.34 to 1.66 m wide. This deposit has a total resource of 6.77 Mt of ore containing >1754 t Ag with an average grade of 284 g/t, 0.38 Mt Pb with an average grade of 5.60 wt% and 0.19 Mt Zn with an average grade of 2.82 wt% (Smith et al., 2020).

Hydrothermal alteration is distributed symmetrically on the two sides of each mineralized vein and is characterized by an assemblage of

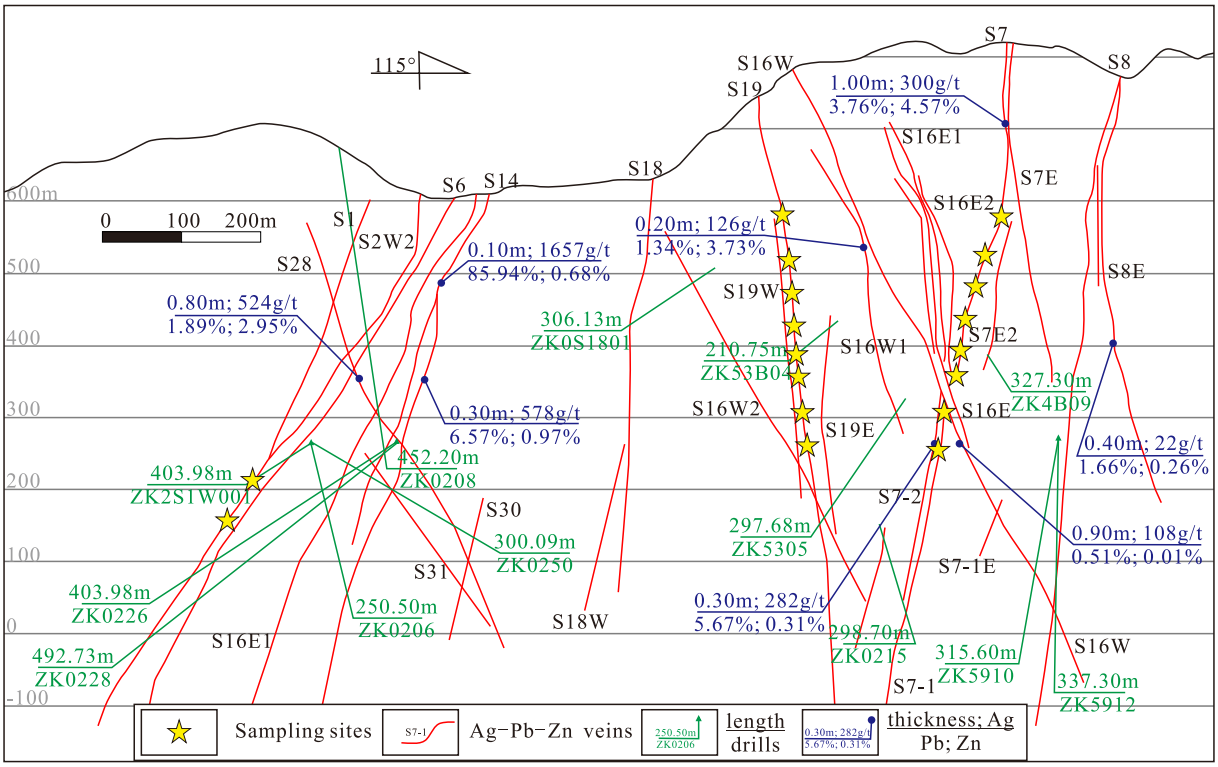

Fig. 3. Cross section along the No. 2 prospecting line of the Shagou deposit (after Stephenson et al., 2016; Smith et al., 2020).

Table 1
A Summary of the Geometrical Features and Metal Contents of Major Ag-Pb-Zn Veins in the Shagou Deposit.

Vein no.	Strike	Dip	Vein					Orebody			Grade		
			Length (m)	Depth (m)	Elevation (m)	Thickness (m)	Average thickness (m)	Number	Length (m)	Thickness (m)	Ag(g/t)	Pb(%)	Zn(%)
S2	265-315°	75-88°	1100	806	660-(−140)	0.30–2.07	0.51	7	35–59	0.51–1.13	212–988	1.67–20.05	1.82–4.9
S2W	310°	80°	400	192	517–360	0.30–0.91	0.33	2	48–62	0.63–0.95	143–587	3.61–14.62	3.83–4.43
S4	300-320°	55-85°	700	602	516-(−50)	0.30–0.84	0.4	2	65–75	0.45–0.5	290–312	2.43–3.55	7.28–7.62
S6	280-305°	65-75°	1160	745	600-(−100)	0.30–1.07	0.37	3	25–85	0.34–0.5	116–352	1.49–5.31	1.46–5.78
S7	112-118°	85°	3000	1032	998-(−30)	0.30–2.37	0.62	4	53–127	0.84–1.43	187–595	2.44–6.6	0.41–4.31
S7-1	290-310°	67-85°	2337	859	745-(−88)	0.30–5.06	0.58	8	45–210	0.91–1.42	236–743	4.67–11.42	2.11–8.82
S8	295-305°	75-82°	3330	771	707-(−50)	0.30–2.01	0.54	4	53–75	0.85–1.41	36–422	4.26–7.76	2.16–6.84
S14	285-305°	73°	1300	758	625-(−100)	0.30–0.96	0.44	3	70–110	0.48–0.76	176–872	5.74–8.65	0.84–1.77
S19	90-312°	70-90°	1800	621	700–100	0.38–6.99	1.25	5	40–100	0.44–1.02	180–430	5.55–7.77	0.19–3.95
S21	295-310°	70-80°	1300	642	770–150	0.30–1.01	0.46	5	40–70	0.76–1.66	348–609	6.55–10.70	0.59–5.97
S21W1	110-120°	70-80°	200	207	600–400	0.30–0.75	0.52	2	40–60	0.97–1.01	371–724	8.16–12.01	1.33–1.41

sericite, chlorite, quartz, and calcite with variable sulfides that occur from the margin toward the center of most veins (Fig. 4A-E). In addition, the host rocks have undergone quartz + sericite ± chlorite hydrothermal alteration, and accompanied the development of pyrite (Fig. 4A-E). Siderite is usually symbiotic with pyrite and quartz, and constituted an early pyrite + quartz ± siderite vein, which were variably eroded, cut, or brecciated and then cemented by the main mineralized veins (Fig. 4A-C). The main Ag-Pb-Zn mineralization is accompanied by extensive quartz alteration zones with ankerite alteration, which range from cm-wide to m-wide, particularly around the very high grade and massive ores (up to 10 m) (Fig. 4A-K). A variety of sulfides were developed in this main metallogenic stage. The dark brown sphalerite + fine-grained galena ± chalcopyrite veins cut through early quartz + pyrite veins (Fig. 4A-C), or containing quartz + pyrite breccia (Fig. 4A-B), and are cut or surrounded by light brown sphalerite + coarse galena veins (Fig. 4G-H). Narrow quartz-calcite alteration bands (<10 cm width) mainly cut the Ag-Pb-Zn mineralized veins (Fig. 4K-L).

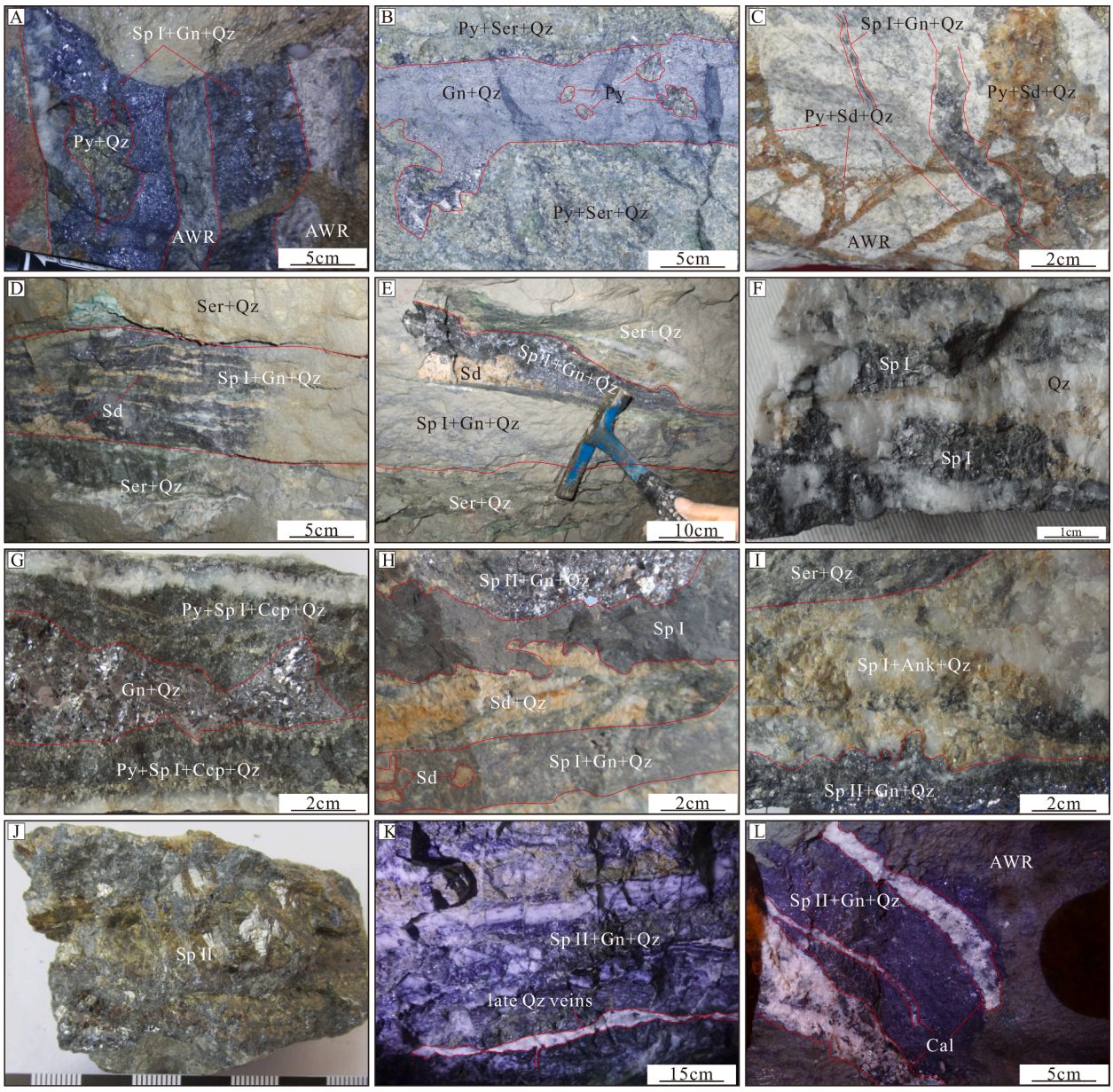

Fig. 4. Photographs of outcrop and hand samples showing textural relations within the Shagou deposit. A. Pb-Zn veins cut across the altered host rock and contain fragments or breccias of pyrite. B. Massive Pb-Zn vein cutting and hosting fragments of the pyrite-sericite-quartz veins. C. Pyrite-sericite-quartz veins cutting altered host rock, in turn cut by Pb-Zn vein, indicating that galena and sphalerite formed late in the paragenesis. D-E. Pb-Zn vein consisting of quartz, siderite, dark-brown sphalerite, and fine galena. Sericite and quartz are well developed on both sides of the vein. F. Coarse-grained, dark-brown sphalerite intergrown with quartz. G. Symmetrical zoning of a Pb-Zn vein consisting of outermost pyrite + dark-brown sphalerite + chalcopyrite + quartz, intermediate coarse galena + quartz. H. Banded textured Pb-Zn ores containing dark-brown sphalerite and light-brown sphalerite. Quartz and siderite were replaced by dark-brown sphalerite, galena, and quartz, indicating that siderite precipitated in the early stages. I. Well-defined mineral zoning consisting of outermost sericite-quartz, intermediate dark-brown sphalerite, fine galena and quartz, and innermost light-brown sphalerite, coarse galena, and quartz. J. Massive coarse-grained light-brown sphalerite. K. Quartz vein with vuggy structure cutting earlier sulfide assemblages. L. Calcite cutting earlier sulfide assemblages. Abbreviations: Ank = ankerite, AHR = altered host rock, Cal = calcite, Ccp = chalcopyrite, Chl = chlorite, Gn = galena, Py = pyrite, Qz = quartz, Sd = siderite, Ser = sericite, Sp = sphalerite.

4. Sampling and analytical methods

More than 60 samples were systemically collected from different Ag-Pb-Zn mineralization veins and mining levels of the Shagou deposit for detailed mineralogical investigation and isotope analysis. The mineral textures, compositions, He-Ar isotope compositions and trace elements of sphalerite were analyzed at the State Key Laboratory of Ore Deposit Geochemistry, Institute of Geochemistry, Chinese Academy of Sciences. In situ Pb isotopes were analyzed at the State Key Laboratory of Continental Dynamics, Northwest University.

4.1. Ore mineral textures and compositions

Forty polished thin sections were examined using reflected and transmitted lights. A JSM-7800F-type thermal field scanning electron microscope coupled with an EDAX TEAM Apollo XL energy-dispersive X-ray spectrometer (EDS) was used to semi-quantitatively identify the compositions and image the textural relationships of the ores. After carbon-coating the slices, elemental point scanning and backscattered electron images were acquired at an acceleration voltage of ~10 kV and a working distance of ~10 mm.

The compositions of the sulfides and sulfosalts were determined

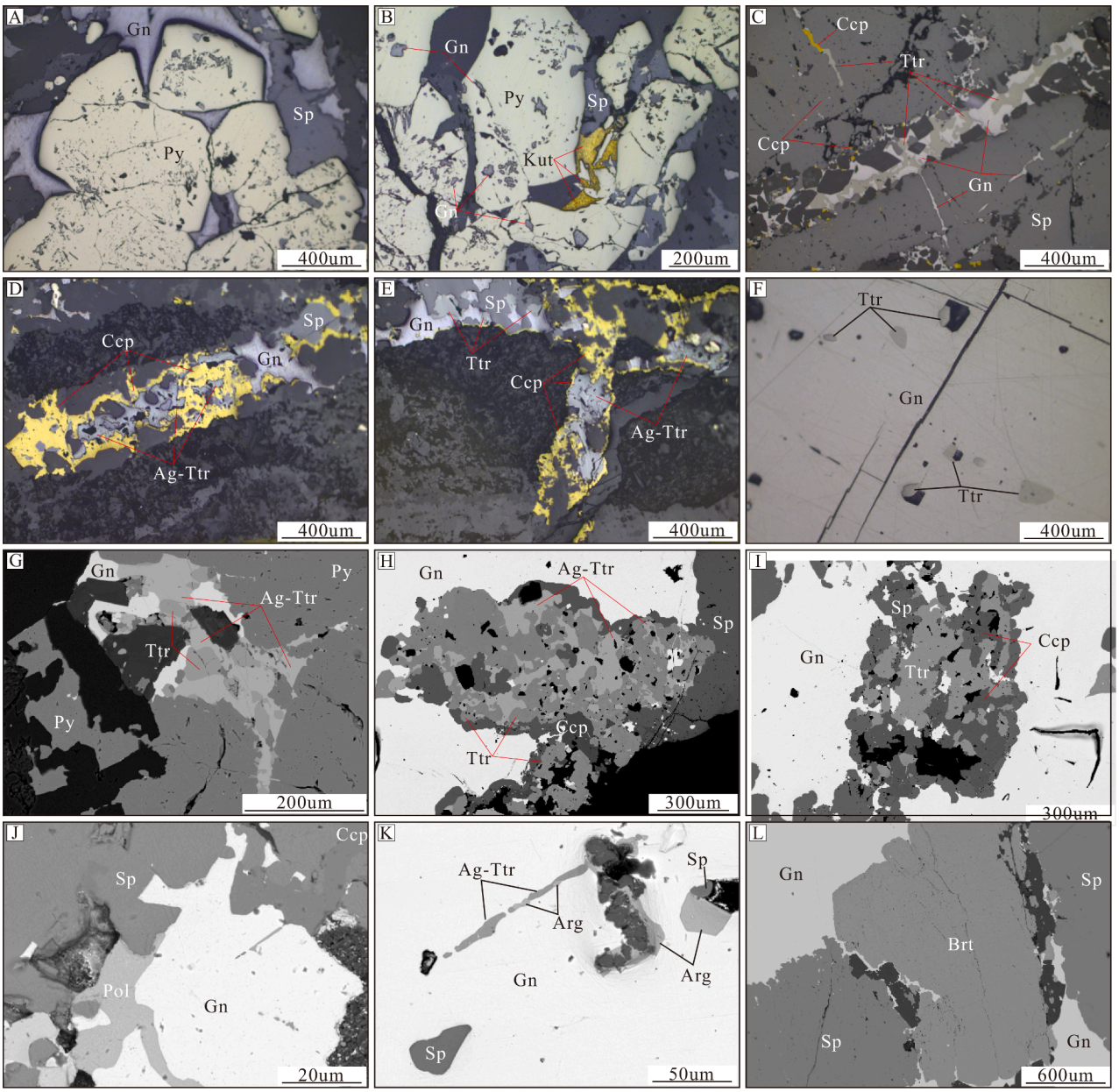

Fig. 5. Reflected-light (A-F) and back-scattered electron (G-L) images illustrating mineralogy and textures of the sulfide ores. A. Coarse-grained, euhedral pyrite was fragmented and then cemented by sphalerite and galena. B. Pyrite contains abundant galena inclusions and was cemented by sphalerite and kustelite. C. Tetrahedrite, galena, and chalcopyrite cut sphalerite. D. Irregular vein containing sphalerite, galena, chalcopyrite and argentiferous tetrahedrite. E. A silver-mineral veinlet containing sphalerite, galena, chalcopyrite, and argentiferous tetrahedrite. F. Tetrahedrite intergrown with galena. G. Galena and coexisting argentiferous tetrahedrite replacing pyrite. H. Tetrahedrite and coexisting argentiferous tetrahedrite are interstitial between sphalerite and galena. Argentiferous tetrahedrite is brighter than tetrahedrite because it contains more Ag. I. Sphalerite and tetrahedrite replacing chalcopyrite, all included in sphalerite. Argentiferous tetrahedrite and polybasite replacing galena, both included in galena. J. Polybasite, galena, and chalcopyrite cutting sphalerite. K. A silver-mineral vein consisting of argentiferous tetrahedrite and argentite within the galena. L. Barite is intergrown with galena and sphalerite. Abbreviations: Ag-Ttr = argentiferous tetrahedrite, Arg = argentite, Brt = Barite, Ccp = chalcopyrite, Gn = galena, Kut = kustelite, Py = pyrite, Pol = polybasite, Sp = sphalerite, Ttr = tetrahedrite.

using a JEOL 8530 Superprobe equipped with wavelength- and energy-dispersive X-ray detectors and a backscatter electron detector; analyses were conducted with an acceleration voltage of ~20 kV, beam current of 10 nA, and 1-μm beam diameter. Natural and synthetic mineral standards and native Ag were used for calibration and were reduced using the ZAF correction method.

4.2. Isotopic geochemistry

Sphalerite and galena (~3 mm) were selected from the crushed ore under a binocular microscope and analyzed for He and Ar isotopes using a GV5400 mass spectrometer following the method of Hu et al. (2012). The mineral grains (~1 g) were cleaned ultrasonically in alcohol, loaded into a vacuo crusher, heated at ~150 °C under ultra-high vacuum for >24 h to remove adhered atmospheric gases, and then subsequentially crushed to extract the volatiles from fluid inclusions. The volatiles were exposed to a titanium-sponge furnace at 800 °C for 20 min to remove active gases (e.g., H_2O), and then flowed through two SAES Zr-Al getters at 250 °C and room temperature, each for 10 min. The remaining gas was exposed to activated charcoal and then cooled using liquid N_2 (~196 °C) for 40 min to separate argon. Air was repeatedly measured and treated as a quality control to determine the mass spectrometer

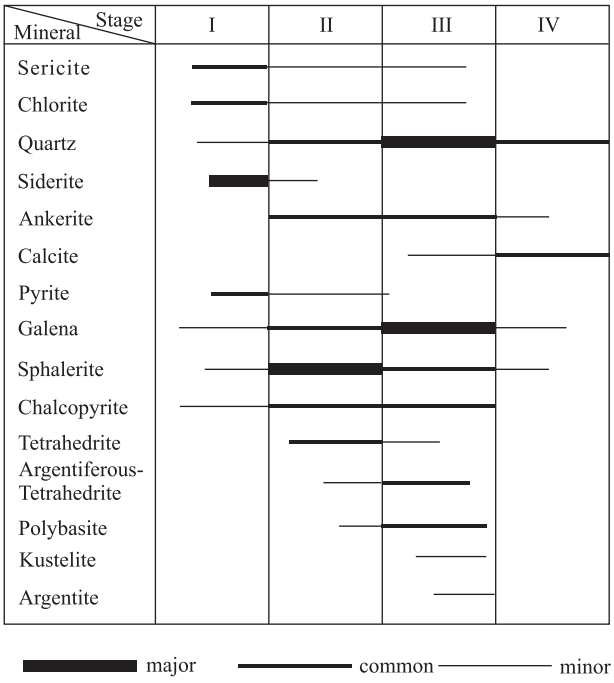

Fig. 6. Paragenetic sequence of the Shagou deposit.

sensitivity and mass fractionation. The crush blanks of ^{4}He and ^{40}Ar were $<2 \times 10^{-10}$ cm^3 STP and $<4 \times 10^{-10}$ cm^3 STP, respectively, which were two orders of magnitude lower than those of the samples and air standard.

In-situ Pb isotope analysis of galena was performed using a RESOlution M-50 laser ablation system (ASI, Australia) connected to a Nu Plasma II MC-ICP-MS (Nu Instruments, Wrexham, UK), following the method of Bao et al. (2017). Helium was used as the carrier gas at an uptake rate of 280 mL/min with a 6 Hz repetition time and 6 J/cm^2 energy density during the laser ablation process. The diameter of the laser ablation beam was 9 um. Each analysis consisted of a background measurement for 30 s, followed by 50 s of ablation for signal collection, and an additional 40 s of wash time to reduce memory effects. ^{205}Tl, ^{204}Hg+^{204}Pb, ^{203}Tl, ^{202}Hg, ^{206}Pb, ^{207}Pb, and ^{208}Pb were collected using L1, L2, L3, L4, Ax, H1, and H2 Faraday cups, respectively. Mass fractionation was corrected by normalizing to $^{205}Tl/^{203}Tl = 2.3889$ using an exponential law. During the analysis, PSPT-2 served as the internal standards, Gn01, and NIST SRM 610 glasses served as the external standards.

4.3. LA-ICP-MS analysis

LA-ICP-MS analyses of sphalerite were conducted using a high-performance RESOlution 193 nm ArF excimer Laser Ablation System coupled to an Agilent 7700x Quadrupole ICP-MS with a beam diameter of 26 μm, repetition time of 6 Hz, and energy density of 6 J/cm^2. Helium was used as the carrier gas to transport the ablated aerosol and was mixed with Ar in a cyclone coaxial mixer before entering the ICP-MS. Each analysis consisted of a 30 s background measurement and 60 s of ablation for signal collection. The following isotopes were monitored: ^{23}Na, ^{34}S, ^{55}Mn, ^{57}Fe, ^{59}Co, ^{60}Ni, ^{65}Cu, ^{66}Zn, ^{71}Ga, ^{72}Ge, ^{75}As, ^{107}Ag, ^{111}Cd, ^{115}In, ^{118}Sn, ^{121}Sb, ^{201}Hg, ^{202}Hg, ^{205}Tl, and ^{208}Pb. During the analysis, in-house sulfide standards GSD-1G, FeSb, and QC-MASS were used to calculate the mass fractions and correct for instrument drift. Data calculations were performed using the LADR software following Longerich et al. (1996). The Zn content of sphalerite was analyzed using EMPA and used as an assumed internal standard during data calculation.

5. Results

5.1. Ore mineralogy and paragenesis

Four Ag-Pb-Zn mineralization stages were identified in the Shagou deposit (Figs. 4–6): (I) early quartz + siderite + pyrite stage, (II) quartz + dark-brown sphalerite + ankerite, (III) quartz + galena + light-brown sphalerite + silver minerals + ankerite, and (IV) late quartz + calcite stage (Fig. 4).

Stage I mainly occurs at the margins of hydrothermal veins and is characterized by a mineral assemblage of quartz + siderite + pyrite accompanied by sericite and chlorite alteration (Fig. 4A-C). This assemblage was crosscut by and included as fragments in later ore veins (Fig. 4A-B). Stage I pyrite is disseminated and euhedral (Fig. 5A-B).

Stage II occurs in the outer part of Ag-Pb-Zn mineralization veins and is characterized by an ore mineral assemblage of galena + sphalerite + pyrite + chalcopyrite ± tetrahedrite with an alteration/gangue assemblage of quartz + ankerite (Fig. 4D-G). Galena is relatively fine-grained. Sphalerite is dark brown, coarse grained, and generally contains abundant inclusions of chalcopyrite (Fig. 4D-F, 5C). This is the main stage of abundant sulfide deposition with minor Ag mineralization.

Stage III occurs in the central part of Ag-Pb-Zn mineralization veins and is characterized by an ore mineral assemblage of galena + sphalerite + silver minerals and an alteration/gangue assemblage of quartz + ankerite + barite (Fig. 4E-J). Galena is relatively coarse grained. Sphalerite is light-brown and fine- to medium-grained (Fig. 4E-H). The silver minerals in this stage were argentiferous tetrahedrite, polybasite, argentite, and electrum (Fig. 5B-K). Minor amounts of native silver, sulfanite, and pyrargyrite were also observed (Li et al., 2013). Minor barite intergrew with the galena and sphalerite (Fig. 5L).

The late paragenetic stage IV includes alteration/gangue assemblages of quartz + calcite, which cut the earlier veins (Fig. 4I-J).

The sulfide minerals in the Shagou deposit are dominated by sphalerite and galena with minor amounts of pyrite and chalcopyrite (Figs. 4 and 5). Arsenopyrite and gersdorffite were also observed (Li et al., 2013). The pyrites contain trace amounts of Co, Ni, and As, whereas chalcopyrite contains trace amounts of Zn and Co (Electronic Appendix Table A1). Galena from stages II and III contained minor amounts of Cd and trace amounts of Zn, Cu, and Fe; however, Ag was below the detection limit (bdl) in both stages (Electronic Appendix Table A1). Dark-brown sphalerite has Fe, Cu, and Cd contents ranging from 0.14 to 2.47, bdl to 2.64, and 0.20 to 0.40 wt%, respectively (Electronic Appendix Table A2). Light-brown sphalerite has Fe, Cu, and Cd contents ranging from bdl to 1.07, bdl to 1.18, and 0.31 to 0.49 wt%, respectively. The Ag content was below the detection limit for both types of sphalerite (Electronic Appendix Table A2).

Argentiferous tetrahedrite and polybasite are the most abundant Ag-bearing ore minerals in the deposit (Fig. 5C-K). They occur as irregular veinlets or stringers in base metal sulfides (Fig. 5C-E), inclusions in galena (Fig. 5F), or aggregate masses within galena (Fig. 5 G-I), showing that these Ag-bearing minerals precipitated after the base metal sulfides.

The EPMA results reveal that tetrahedrite has Ag, Cu, Zn, Fe, Sb, As, and S contents ranging from 6.94 to 7.72, 32.84 to 33.20, 6.76 to 6.83, 0.62 to 0.64, 26.25 to 26.31, 1.93 to 2.03, and 23.70 to 23.87 wt%, respectively (Electronic Appendix Table A1). Argentiferous tetrahedrite is relatively enriched in Ag than tetrahedrite, and contains Ag, Cu, Zn, Fe, Sb, As, and S contents ranging from 8.89 to 19.83, 23.33 to 32.63, 5.79 to 7.80, 0.61 to 1.87, 20.58 to 27.45, 0.93 to 5.43, and 22.65 to 24.22 wt%, respectively (Electronic Appendix Table A1). Ag, Cu, Sb, As, and S contents of polybasite range from 64.02 to 76.25, 2.21 to 9.79, 5.36 to 9.90, 0.16 to 3.41, and 12.87 to 16.25 wt%, respectively. There are also minor to trace amounts of Zn (up to 0.38 wt%) and Fe (up to 0.76 wt%) (Electronic Appendix Table A1).

Several kustelite grains can be observed at the edge of the pyrite (Fig. 5B), containing Au and Ag ranging from 49.49 to 56.03, and 39.19 to 46.90 wt%, respectively (Electronic Appendix Table A1).

Table 2
He and Ar isotopic compositions of the sulfides from the Shagou Deposit.

Sample	Mineral	Weight	^{4}He (ccSTP)	^{3}He (ccSTP)	R(Ra)	^{40}Ar (ccSTP)	^{36}Ar (ccSTP)	^{40}Ar/^{36}Ar	^{40}Ar*/^{4}He	^{3}He/^{36}Ar	^{40}Ar/^{36}Ar	^{3}He/^{36}Ar
350-3-1	Sphalerite	0.351	3.14E-06	1.57E-12	0.36	5.59E-07	9.21E-10	607.20	0.10	1.70E-03	607.20	3.40E + 03
300-5	Sphalerite	0.307	5.59E-06	2.44E-12	0.31	8.37E-07	7.79E-10	1073.42	0.11	3.13E-03	1073.42	7.18E + 03
300-2	Galena	0.312	1.76E-06	6.23E-13	0.25	3.10E-07	1.92E-10	1609.27	0.04	3.24E-03	1609.27	9.16E + 03
260-1	Sphalerite	0.276	1.50E-05	8.57E-12	0.41	1.67E-06	6.87E-10	2431.02	0.09	1.25E-02	2431.02	2.18E + 04
350-4	Galena	0.127	5.97E-07	6.14E-13	0.74	2.19E-07	2.23E-10	981.62	0.14	2.75E-03	981.62	2.67E + 03
490-3	Sphalerite	0.243	2.41E-06	8.82E-13	0.26	2.80E-07	6.37E-10	439.31	0.26	1.38E-03	439.31	3.78E + 03

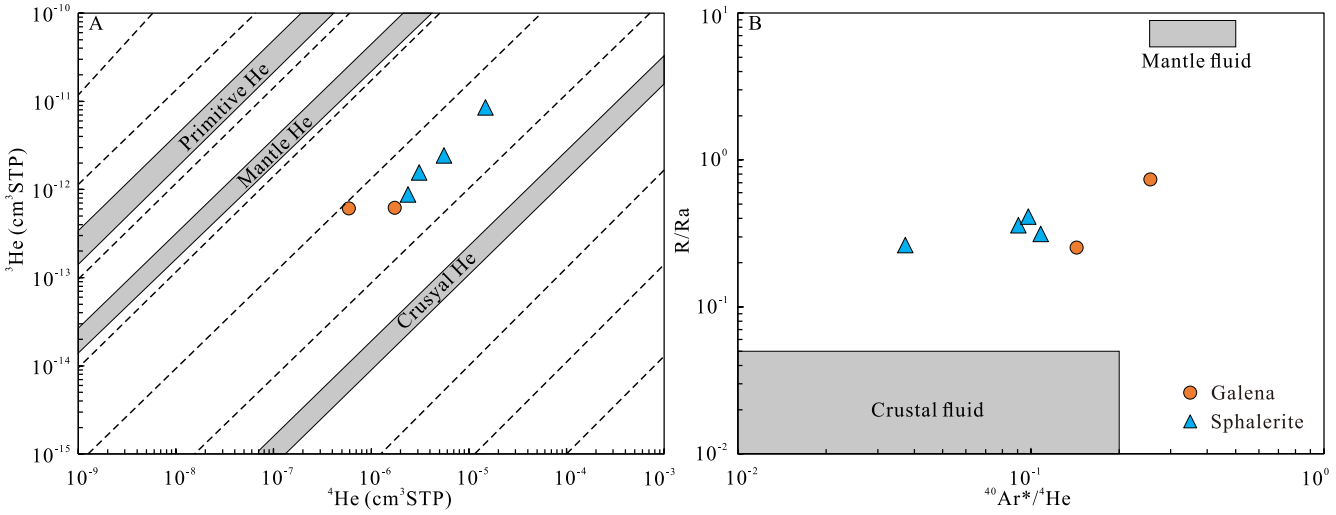

Fig. 7. He-Ar isotopic compositions of sulfide from the Shagou deposit.

5.2. He-Ar-Pb isotopic compositions

The ^{4}He and ^{40}Ar of sphalerite range from 2.4 × 10^{-6} to 1.5 × 10^{-5} cm^3 STP g^{-1}, and 2.8 × 10^{-7} to 1.7 × 10^{-6} cm^3 STP g^{-1}, respectively (Table 2). Those of galena vary from 6.0 × 10^{-7} to 1.8 × 10^{-6} cm^3 STP g^{-1}, and 2.2 × 10^{-7} to 3.1 × 10^{-7} cm^3 STP g^{-1}, respectively (Table 2). The large range of ^{4}He and ^{40}Ar content in sphalerite and galena is likely related to the volume of fluid inclusions and the crushing efficiency. ^{3}He/^{4}He ratios of the ore fluids range from 0.26 to 0.41 Ra for sphalerite and 0.25 to 0.74 Ra for galena. ^{40}Ar/^{36}Ar ratios vary from 439 to 2431 for sphalerite and from 982 to 1609 for galena (Table 2, Fig. 7).

The Pb isotope values of galena were similar and largely independent of depth in the Shagou deposit. The ^{206}Pb/^{204}Pb, ^{207}Pb/^{204}Pb, and ^{208}Pb/^{204}Pb ratios range from 17.448 to 17.858, 15.479 to 15.530, and 38.380 to 38.612, with mean ratios of 17.666, 15.506, and 38.510, respectively (Table 3). The ^{206}Pb/^{204}Pb ratio exhibited a linear relationship with the ^{208}Pb/^{204}Pb (R^2 = 0.97; Fig. 8A) and ^{207}Pb/^{204}Pb ratios (R^2 = 0.93; Fig. 8B).

5.3. Trace elements in sphalerite

Trace element compositions of dark-brown sphalerite (44 spots) and light-brown sphalerite (40 spots) were analyzed using LA-ICP-MS and are listed in Table 4 (detailed data are listed in Electronic Appendix Table A2). The LA-ICP-MS ablation profiles were generally smooth without abnormal Na peaks, indicating that the elements were homogeneously distributed in the sphalerite and were not affected by fluid inclusions (Fig. 9). The results showed that dark- and light-brown sphalerites have different trace element compositions (Fig. 10).

Fe and Cu contents in dark-brown sphalerite (mean = 5035 and 3825 ppm, respectively) were higher than those in the light-brown variety (mean = 688 and 594 ppm, respectively), whereas the Cd content showed a similar distribution in dark-brown (mean = 2465 ppm) and light-brown sphalerite (mean = 3062 ppm).

Ag concentrations generally decreased from stage II to stage III, with an average of 145 ppm for dark-brown and 99.8 ppm for light-brown sphalerite. In contrast, the average concentration of In increased from dark-brown (average 62.0 ppm) to light-brown sphalerite (average 97.5 ppm). The Mn and Ni concentrations were mostly below the detection limit in the light-brown sphalerite, but relatively enriched in the dark-brown sphalerite, with an average of 11.3 and 0.882 ppm, respectively. Co, As, Sb, and Pb contents remained similar from stage II to stage III, ranging from 0.372 to 85.4 ppm, < bdl to 39.5 ppm, < bdl to 298 ppm, and < bdl to 323 ppm, respectively. Ga, Ge, and Sn contents vary by more than two orders of magnitude (<bdl to 33.2 ppm, < bdl to 28.8 ppm, < bdl to 1114 ppm, respectively), and are relatively enriched in dark-brown sphalerite, with mean values of 7.06 ppm, 3.06 ppm, and 186 ppm, respectively.

6. Discussion

6.1. Sources of ore-forming materials

He and Ar in ore-forming fluids are mainly sourced from air-saturated water, mantle-derived volatiles, and the radiogenic decay of U, Th, and K in crustal rocks (Turner et al., 1993; Stuart et al., 1995). He has an extremely low abundance in the atmosphere and low solubility in aqueous fluids (Stuart et al., 1995), thus mantle-derived He and radiogenic He produced in the crust are two possible sources of He in hydrothermal fluids (Turner et al., 1993). The ^{3}He/^{36}Ar ratios of the Shagou deposit (1.38–12.48 × 10^{-3}) are more than 5 orders of magnitude higher than the value for air-saturated water (~5 × 10^{-8}), and the F^{4}He values (16,157–13,1722) are also more than 5 orders of magnitude higher than the value for the atmosphere (F^{4}He = 1; Kendrick et al., 2001), indicating negligible atmospheric He in the ore-forming fluids of the Shagou deposit.

^{3}He/^{4}He values of mantle-derived fluids are higher than 0.05 Ra (O'Nions and Oxburgh, 1983). The ^{3}He/^{4}He values of sphalerite and

Table 3
In Situ Lead Isotope Results of Galena from the Shagou Deposit.

Analysis spot	$^{208}Pb/^{204}Pb$	SE	$^{207}Pb/^{204}Pb$	SE	$^{206}Pb/^{204}Pb$	SE	$^{208}Pb/^{206}Pb$	SE	$^{207}Pb/^{206}Pb$	SE	Pb Beam	SE	$^{204}Hg/^{204}Pb$	SE
sg300-6-1-C1-gn1	38.432	0.004	15.494	0.001	17.517	0.002	2.1940	0.0000	0.8846	0.0000	19.63	0.66	0.000	0.000
sg300-6-1-C1-gn2	38.434	0.004	15.495	0.002	17.519	0.002	2.1939	0.0001	0.8845	0.0000	16.57	0.59	0.000	0.000
sg300-6-1-C2-gn1	38.435	0.004	15.496	0.001	17.519	0.001	2.1940	0.0001	0.8845	0.0000	18.70	0.71	0.000	0.000
sg300-6-1-C2-gn2	38.440	0.004	15.498	0.002	17.523	0.002	2.1938	0.0001	0.8844	0.0000	18.13	0.68	0.000	0.000
sg300-6-1-C2-gn3	38.442	0.005	15.498	0.002	17.524	0.002	2.1936	0.0001	0.8844	0.0000	17.92	0.72	0.000	0.000
sg350-5-C5-gn1	38.384	0.014	15.485	0.005	17.450	0.005	2.1997	0.0002	0.8874	0.0001	35.32	0.92	0.000	0.000
sg350-5-C5-gn2	38.388	0.013	15.486	0.005	17.449	0.004	2.2000	0.0002	0.8875	0.0000	35.61	0.85	0.000	0.000
sg350-5-C5-gn3	38.383	0.013	15.485	0.004	17.448	0.004	2.2000	0.0002	0.8875	0.0000	44.77	0.71	0.000	0.000
sg350-5-C6-gn1	38.393	0.013	15.486	0.005	17.455	0.004	2.1996	0.0002	0.8872	0.0000	46.86	0.91	0.000	0.000
sg350-5-C6-gn2	38.380	0.012	15.481	0.004	17.449	0.004	2.1996	0.0002	0.8873	0.0000	49.55	0.70	0.000	0.000
18sg-10-C1-gn1	38.509	0.010	15.501	0.003	17.615	0.003	2.1862	0.0001	0.8801	0.0000	27.09	0.68	0.000	0.000
18sg-10-C1-gn2	38.516	0.011	15.503	0.004	17.618	0.004	2.1863	0.0002	0.8801	0.0000	28.68	0.64	0.000	0.000
18sg-10-C1-gn3	38.518	0.011	15.505	0.004	17.618	0.004	2.1863	0.0002	0.8801	0.0000	27.14	0.80	0.000	0.000
18sg-10-C2-gn1	38.524	0.013	15.505	0.005	17.618	0.004	2.1865	0.0002	0.8801	0.0000	53.03	1.12	0.000	0.000
18sg-10-C2-gn2	38.497	0.012	15.496	0.004	17.610	0.004	2.1861	0.0002	0.8801	0.0000	56.89	1.43	0.000	0.000
sg400-C2-gn2	38.444	0.007	15.496	0.003	17.539	0.002	2.1920	0.0001	0.8835	0.0000	19.31	0.75	0.000	0.000
sg400-C3-gn1	38.487	0.016	15.502	0.006	17.642	0.007	2.1814	0.0001	0.8789	0.0000	2.01	0.07	0.000	0.000
sg400-C3-gn2	38.448	0.007	15.494	0.003	17.567	0.003	2.1887	0.0001	0.8821	0.0000	15.51	0.37	0.000	0.000
sg400-C1-gn1	38.612	0.003	15.529	0.001	17.858	0.001	2.1622	0.0000	0.8696	0.0000	16.39	0.50	0.000	0.000
sg400-C1-gn2	38.597	0.005	15.523	0.002	17.854	0.002	2.1621	0.0001	0.8696	0.0000	16.62	0.46	0.000	0.000
sg400-C2-gn1	38.612	0.003	15.529	0.001	17.855	0.001	2.1626	0.0000	0.8697	0.0000	16.86	0.55	0.000	0.000
sg400-C2-gn2	38.600	0.003	15.525	0.001	17.851	0.001	2.1624	0.0000	0.8697	0.0000	18.42	0.55	0.000	0.000
sg400-C2-gn3	38.610	0.005	15.528	0.002	17.856	0.002	2.1623	0.0001	0.8697	0.0000	18.66	0.48	0.000	0.000
sg530-5-C2-gn1	38.387	0.003	15.480	0.001	17.475	0.001	2.1965	0.0000	0.8858	0.0000	17.32	0.45	0.000	0.000
sg530-5-C2-gn2	38.384	0.003	15.479	0.001	17.475	0.001	2.1964	0.0000	0.8858	0.0000	16.71	0.45	0.000	0.000
sg530-5-C3-gn1	38.385	0.004	15.480	0.002	17.473	0.002	2.1967	0.0001	0.8859	0.0000	18.06	0.66	0.000	0.000
sg530-5-C3-gn2	38.409	0.004	15.487	0.001	17.481	0.001	2.1971	0.0001	0.8859	0.0000	19.86	0.62	0.000	0.000
sg530-5-C3-gn3	38.401	0.005	15.485	0.002	17.479	0.002	2.1970	0.0001	0.8860	0.0000	19.26	0.68	0.000	0.000
sg260-C2-sp2	38.625	0.045	15.519	0.017	17.908	0.020	2.1577	0.0002	0.8665	0.0001	0.74	0.04	0.018	0.001
sg490-3-1-C2-gn1	38.523	0.003	15.504	0.001	17.727	0.001	2.1732	0.0001	0.8747	0.0000	14.41	0.39	0.000	0.000
sg490-3-1-C1-gn1	38.537	0.003	15.509	0.001	17.739	0.001	2.1725	0.0000	0.8744	0.0000	14.83	0.41	0.000	0.000
sg490-3-1-C1-gn2	38.529	0.004	15.506	0.001	17.737	0.001	2.1722	0.0000	0.8743	0.0000	14.90	0.34	0.000	0.000
sg490-3-1-C1-gn3	38.522	0.003	15.504	0.001	17.733	0.001	2.1723	0.0000	0.8743	0.0000	14.69	0.40	0.000	0.000
260-1-gn1	38.677	0.006	15.539	0.002	17.941	0.002	2.1556	0.0001	0.8661	0.0000	14.52	0.57	0.000	0.000
260-1-gn2	38.674	0.005	15.539	0.002	17.942	0.002	2.1554	0.0001	0.8661	0.0000	14.70	0.57	0.000	0.000
260-1-gn3	38.674	0.006	15.539	0.002	17.943	0.002	2.1553	0.0001	0.8661	0.0000	13.45	0.57	0.000	0.000
260-1-gn4	38.689	0.004	15.545	0.002	17.945	0.002	2.1558	0.0001	0.8662	0.0000	13.63	0.50	0.000	0.000
260-1-gn5	38.683	0.005	15.544	0.002	17.946	0.002	2.1554	0.0001	0.8662	0.0000	10.45	0.42	0.000	0.000
300-2-gn1	38.282	0.004	15.442	0.002	17.202	0.002	2.2254	0.0001	0.8977	0.0000	12.49	0.31	0.000	0.000
300-2-gn2	38.290	0.004	15.443	0.002	17.201	0.002	2.2258	0.0001	0.8978	0.0000	12.92	0.33	0.000	0.000
300-2-gn3	38.297	0.004	15.445	0.001	17.237	0.002	2.2216	0.0001	0.8960	0.0000	12.44	0.33	0.000	0.000
300-2-gn4	38.294	0.004	15.446	0.002	17.232	0.002	2.2221	0.0001	0.8963	0.0000	11.13	0.29	0.000	0.000
300-2-gn5	38.275	0.004	15.439	0.001	17.196	0.002	2.2256	0.0001	0.8978	0.0000	11.99	0.36	0.000	0.000
350-5-gn1	38.572	0.005	15.517	0.002	17.807	0.002	2.1659	0.0001	0.8713	0.0000	12.19	0.42	0.000	0.000
350-5-gn2	38.581	0.005	15.520	0.002	17.812	0.002	2.1658	0.0001	0.8713	0.0000	12.82	0.40	0.000	0.000
350-5-gn3	38.600	0.004	15.530	0.002	17.823	0.002	2.1657	0.0001	0.8713	0.0000	12.23	0.42	0.000	0.000

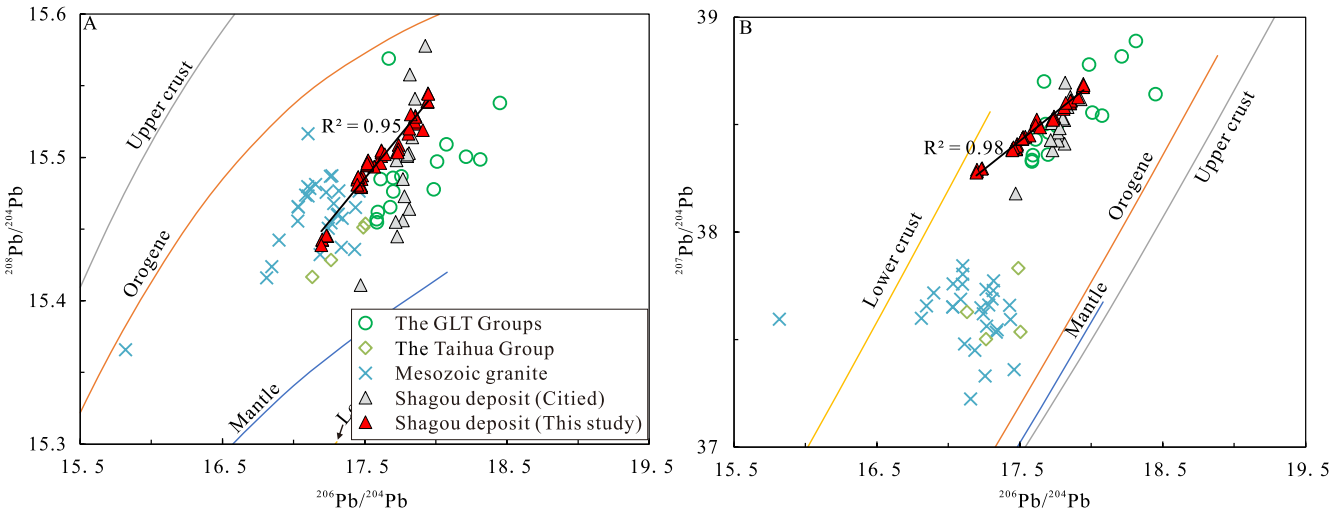

Fig. 8. Pb isotopic compositions of galena from the Shagou deposit.

galena from the Shagou deposit range from 0.25 to 0.74 Ra, with a mean value of 0.42 Ra (Table 2; Fig. 7), which is significantly higher than those of the crust (0.01 to 0.05Ra; O'Nions and Oxburgh, 1983), but notably lower than those of the mantle (6 to 9 Ra; Graham, 2002; Gautheron and Moreira, 2002), indicating a contribution from a mantle-derived He flux. In addition, the $^{40}Ar/^{36}Ar$ values of the Shagou deposit range from 439 to 2431, with a mean value of 1252 (Table 2), which is markedly higher than that of the atmosphere (298.6; Lee et al., 2006), and lower than that of the mantle (10,000 to 40,000; Burnard et al., 1999). $^{3}He/^{40}Ar^{*}$ ratios range from 2.4 to 9.8 × 10^{-6}, lower than that of mantle (~10^{-4}, Kennedy et al., 1991), and higher than that of the crust (~10^{-8}, Kennedy et al., 1991). These values suggest that the ore-forming fluids of the Shagou deposit were derived from a mix of crustal and mantle sources. This conclusion is also supported by previous chronological studies. Xenotime U-Pb dating suggest the Ag-Pb-Zn mineralization age of 123.3 ± 1.7 Ma from the Shagou deposits, which is consistent with the emplaced age of granite porphyry in Haopinggou intrusion within the error range (125.9 ± 0.7 Ma; Tian et al., 2023).

To evaluate the source of the metals, we compared the Pb isotopic compositions of the Shagou deposit with corresponding data from contemporary granites (Li et al., 2018 and references therein), the Taihua Group (Ni et al., 2012), and the GLT Groups (Qi, 2006), which all have U, Th, and Pb contents and isotopes. The corresponding data were corrected for the age of the Shagou deposit (~123 Ma, Tian et al., 2023). Based on $^{206}Pb/^{204}Pb$ vs. $^{207}Pb/^{204}Pb$ and $^{206}Pb/^{204}Pb$ vs. $^{208}Pb/^{204}Pb$ diagrams, the Pb isotope ratios for the Shagou ores plot between those of contemporary granites and the GLT Groups (Fig. 8; Zartman and Doe, 1981), suggesting that the Pb and other metals (e.g., Ag and Zn) were sourced from both rock types. Metals may have been partly leached from the Taihua Group, which experienced intense hydrothermal alteration.

Based on the He-Ar-Pb isotope results of this study and previous chronological results suggest that the Shagou deposit is closely related to contemporaneous magmatism, and the deep magmatic fluid extracted Pb and other metals (e.g., Ag and Zn) from the GLT groups during the upward process, and when the ore-forming fluid enters NE- to NNE-striking faults, the mineralizing elements are further extracted from the surrounding Taihua group due to the water–rock reaction.

6.2. Mechanisms of Ag precipitation

Crosscutting relationships demonstrate that the base metals and Ag mineralization mainly precipitated in stages II and III, in which sphalerite and freibergite are representative ore mineral assemblages, respectively. Previous studies have demonstrated that sphalerite compositions provide a useful guide for revealing the physicochemical environment of ore formation (Scott and Barnes, 1971; Frenzel et al., 2016). The sphalerites in the Shagou deposit are mostly dark brown and light brown in color, with an Fe content of up to 3.01 wt%, similar to those formed under intermediate- to low-temperature conditions (Kelley et al., 2004).

The average Ag concentration generally decreased from dark-brown sphalerite (145 ppm) to light-brown sphalerite (99.8 ppm), suggesting that Ag precipitated significantly from stage II to stage III and formed silver minerals. The concentrations of In, Fe, Mn, Ga, and Ge in sphalerite are positively related to the formation temperature of the base metal (Frenzel et al., 2016). The dark-brown sphalerites were enriched In, Fe, Mn, Ga, and Ge relative to the light-brown type. Applying the GGIMFis geothermometer to the base metal and silver mineralization yields temperatures of 153 to 263 ℃ (mean ~ 207 ℃) and 132 to 240 ℃ (mean ~ 190 ℃), respectively (Frenzel et al., 2016). These temperatures are similar to the homogeneous temperature of fluid inclusions hosted in the same mineral assemblages, which are from 157 to 267 °C (mean ~209 ℃) for the base metal sulfide and from 160 to 210 °C (mean ~190 ℃) for silver mineralization (Li et al., 2013). Therefore, ore deposition in the Shagou deposit was initiated at a moderate temperature (~207 °C), but progressively evolved to lower temperature conditions (~190 °C), coeval with the precipitation of silver (Fig. 11).

The corresponding logfS_2 values of dark-brown and light-brown sphalerites range from −14.5 to −8.3 (average of −11.5) and from −15.6 to −9.5 (average of −12.3) (Scott and Barnes, 1971), indicating that the Shagou deposit was formed in an intermediate-sulfidation hydrothermal system (Einaudi et al., 2005), and that S fugacity decreased as the temperature reduced during Ag deposition (Fig. 12). The constrained logfO_2 values of dark-brown and light-brown sphalerites range from −38.7 to −29.4 (average of −34.2) and from −40.5 to −31.2 (average of −35.4) (Scott and Barnes, 1971), suggesting that the hydrothermal system transformed to decreasing logfO_2 conditions from base metal sulfide to silver mineralization.

Siderite and sericitic alterations in Stage I were widespread in the Shagou veins, and calcite was deposited in the later stage, indicating that the ore-forming fluids transformed from early acidic to late near-neutral conditions (Stoffregen, 1987). Fluid inclusion studies have demonstrated that early ore fluids are characterized by Cl^{-} (Gao et al., 2010; Li et al., 2013; Han et al., 2014), indicating that silver and other metals were transported as chloride species in early hydrothermal systems (Seward, 1976; Gammons and Barnes, 1989). As the hydrothermal fluid ascended along NE- to NNE trending faults, reduction of sulfur and oxygen fugacity reduced Cl^{-} solubility in the fluid, resulting in silver and other metals being transported by bisulfide species (Stefansson and

Table 4
Summary LA-ICP-MS results of sphalerite from the Shagou deposit.

Sample name	Type		^{55}Mn	^{57}Fe	^{59}Co	^{60}Ni	^{65}Cu	^{71}Ga	^{72}Ge	^{75}As	^{107}Ag	^{111}Cd	^{115}In	^{118}Sn	^{121}Sb	^{208}Pb	T/°C[1]	logfS_2	logfO_2
530-4-sp-c1	Light brown	Min	–	77.0	8.77	0.514	13.4	0.0486	0.821	0.342	57.1	3020	0.0400	0.184	2.23	26.0	–	–	–
		Max	1.67	938	43.9	16.9	62.0	1.92	2.08	6.41	180	4050	3.04	6.75	43.9	80.1	132	−15.64	−40.46
		Median	–	305	22.9	4.45	31.0	0.614	1.33	3.22	104	3430	0.863	2.07	17.6	52.6	–	–	–
		S.D.	–	247	13.0	5.62	15.6	0.559	0.398	2.37	32.8	338	1.00	1.99	14.1	16.9	–	–	–
		Count	1	10	10	2	10	10	10	4	10	10	9	7	10	10	1	1	1
530-4-sp-c2	Dark-brown	Min	2.66	2650	1.20	0.609	578	1.95	0.602	0.420	108	1620	14.9	22.5	2.93	15.3	197	−11.97	−34.95
		Max	25.7	6580	17.4	2.16	6370	17.3	1.48	5.03	354	2700	161	204	65.7	323	248	−9.12	−30.68
		Median	9.55	4660	6.34	1.24	2750	9.80	0.970	2.25	195	2080	76.1	113	29.8	103	213	−11.11	−33.67
		S.D.	8.47	1120	4.52	0.590	1660	5.33	0.265	1.70	70.0	322	35.9	45.0	18.5	83.6	16	0.90	1.36
		Count	10	10	10	3	10	10	8	10	10	10	10	10	10	10	7	7	7
450-3-sp-c2	Light brown	Min	2.05	443	14.8	0.601	32.2	0.0389	0.558	0.451	45.0	2540	0.535	0.399	1.97	7.48	182	−12.60	−35.90
		Max	26.4	6530	76.7	2.02	7760	3.66	1.65	5.87	202	2820	49.3	10.1	145	83.7	240	−9.46	−31.18
		Median	13.8	2090	42.2	1.11	2110	1.18	1.01	2.21	97.5	2700	17.1	4.16	37.8	32.9	213	−10.98	−33.46
		S.D.	10.0	1890	20.4	0.592	2410	1.09	0.340	1.82	48.5	86.8	16.2	3.33	44.8	24.0	24	1.29	1.93
		Count	3	8	8	4	8	8	8	7	8	8	8	8	8	8	3	3	3
300-5-sp-c1	Dark-brown	Min	–	465	27.8	–	13.4	0.0875	0.628	1.26	25.6	3000	0.0443	0.364	1.10	6.60	–	–	–
		Max	2.20	1110	85.4	–	430	2.29	1.83	2.95	99.8	3140	0.469	1.21	29.8	36.7	153	−14.50	−38.74
		Median	–	720	46.0	–	140	1.08	1.11	2.10	55.4	3060	0.196	0.766	8.77	19.3	–	–	–
		S.D.	–	226	17.9	–	143	0.745	0.507	0.846	22.4	49.6	0.151	0.348	9.49	9.69	–	–	–
		Count	1	7	7	0	7	5	6	2	7	7	6	3	7	7	1	1	1
490-7-sp-c2	Dark-brown	Min	2.01	1840	9.23	–	1880	1.56	1.26	4.07	159	2580	54.7	46.5	40.3	31.1	175	−13.13	−36.70
		Max	50.6	5690	27.1	–	7170	33.2	28.8	39.5	404	2880	205	1110	209	212	177	−12.90	−36.35
		Median	26.3	3760	16.8	–	4420	14.0	10.4	15.0	275	2730	118	565	94.9	94.9	176	−13.02	−36.52
		S.D.	24.3	1560	6.51	–	2110	11.2	10.2	13.7	93.8	116	52.6	461	63.5	65.9	1	0.11	0.17
		Count	2	5	5	0	5	5	5	5	5	5	5	5	5	5	2	2	2
350-5-sp-c6	Dark-brown	Min	4.95	3420	4.49	–	13.6	0.741	0.548	2.13	10.1	2150	0.103	0.445	0.428	3.69	181	−12.89	−36.33
		Max	9.94	6420	29.6	–	6920	9.22	3.23	6.55	70.4	2830	12.2	44.6	20.0	15.6	212	−11.26	−33.89
		Median	7.16	4840	17.8	–	4420	4.84	1.64	4.34	37.7	2510	4.13	12.6	5.84	9.72	195	−12.14	−35.21
		S.D.	2.08	840	8.45	–	1840	2.64	0.917	2.21	15.6	215	4.00	14.1	6.29	3.81	13	0.65	0.98
		Count	9	9	9	0	9	9	–	2	9	9	9	9	9	9	6	6	6
570-5-sp-c1	Light brown	Min	–	633	43.1	–	67.1	–	–	1.27	144	2600	47.0	0.323	12.8	45.4	–	–	–
		Max	0.421	886	55.8	5.68	134	1.94	–	2.50	208	2970	73.6	8.69	34.2	2030	–	–	–
		Median	–	518	49.0	–	75.8	–	–	1.71	153	2840	51.1	3.22	19.2	485	–	–	–
		S.D.	–	328	4.90	–	31.1	–	–	0.760	39.6	109	15.3	2.77	11.7	696	–	–	–
		Count	1	7	7	1	7	1	0	6	7	7	7	6	7	7	0	0	0
SG490-3-1-Sp-C3	Light brown	Min	0.422	92.8	16.8	0.241	53.5	0.0273	0.410	0.464	69.9	2950	17.2	13.1	11.4	14.0	–	–	–
		Max	0.423	414	54.8	0.383	358	0.283	0.603	7.10	194	3390	49.8	161	74.8	56.9	184	−12.48	−35.73
		Median	0.423	199	42.1	0.323	176	0.103	0.510	3.95	135	3100	33.0	62.7	41.8	34.5	–	–	–
		S.D.	0.000398	105	11.1	0.0596	100	0.0813	0.0792	2.45	45.9	136	10.6	51.2	22.2	16.3	–	–	–
		Count	2	8	8	3	8	7	3	8	8	8	8	8	8	8	1	1	1
SG490-3-1-Sp-C4	Dark-brown	Min	3.22	7410	0.372	0.799	937	4.45	0.796	10.5	118	1530	10.5	62.8	101	27.8	182	−13.01	−36.52
		Max	26.2	17,600	5.88	1.82	18,500	12.1	4.75	38.9	511	2670	43.8	737	298	207	245	−9.70	−31.56
		Median	11.4	12,300	2.46	1.18	9410	8.47	2.24	21.8	289	2010	27.6	319	172	89.9	222	−10.90	−33.35
		S.D.	8.34	3630	2.09	0.456	6410	2.63	1.39	9.51	117	417	11.2	210	67.0	58.8	22	1.16	1.75
		Count	7	7	7	3	7	7	7	7	7	7	7	7	7	7	7	7	7
350-3-2-Sp-C1	Dark-brown	Min	2.52	1270	6.03	0.292	93.8	0.0871	0.575	0.321	16.8	2610	68.2	4.24	0.148	1.26	222	−10.48	−32.72
		Max	24.9	3470	34.1	0.592	214	2.45	0.584	0.745	49.1	2870	225	80.5	11.7	8.14	263	−8.27	−29.40
		Median	12.6	2260	17.6	0.421	169	0.993	0.580	0.544	32.5	2730	172	44.1	4.16	4.44	243	−9.37	−31.06
		S.D.	8.65	649	11.2	0.0926	43.3	0.798	0.00463	0.174	13.5	95.3	55.0	27.4	3.70	2.51	21	1.11	1.66
		Count	6	6	6	6	6	6	2	3	6	6	6	6	6	6	2	2	2
350-3-2-Sp-C2	Light brown	Min	0.277	120	66.1	0.301	167	0.0245	0.439	0.112	12.6	2970	239	1.66	0.178	0.133	–	–	–
		Max	0.338	201	82.7	0.543	277	0.0667	0.580	0.551	32.3	3270	474	18.0	4.96	6.07	–	–	–
		Median	0.307	151	73.3	0.457	239	0.0450	0.497	0.231	19.7	3080	399	6.45	1.48	1.63	–	–	–
		S.D.	0.0304	27.1	5.09	0.0829	35.6	0.0164	0.0555	0.185	6.19	111	74.2	5.07	2.01	2.02	–	–	–
		Count	2	7	7	7	7	4	5	4	7	7	7	7	4	6	0	0	0

Notes1: T was the GGIMFis geothermometer (Frenzel et al., 2016).

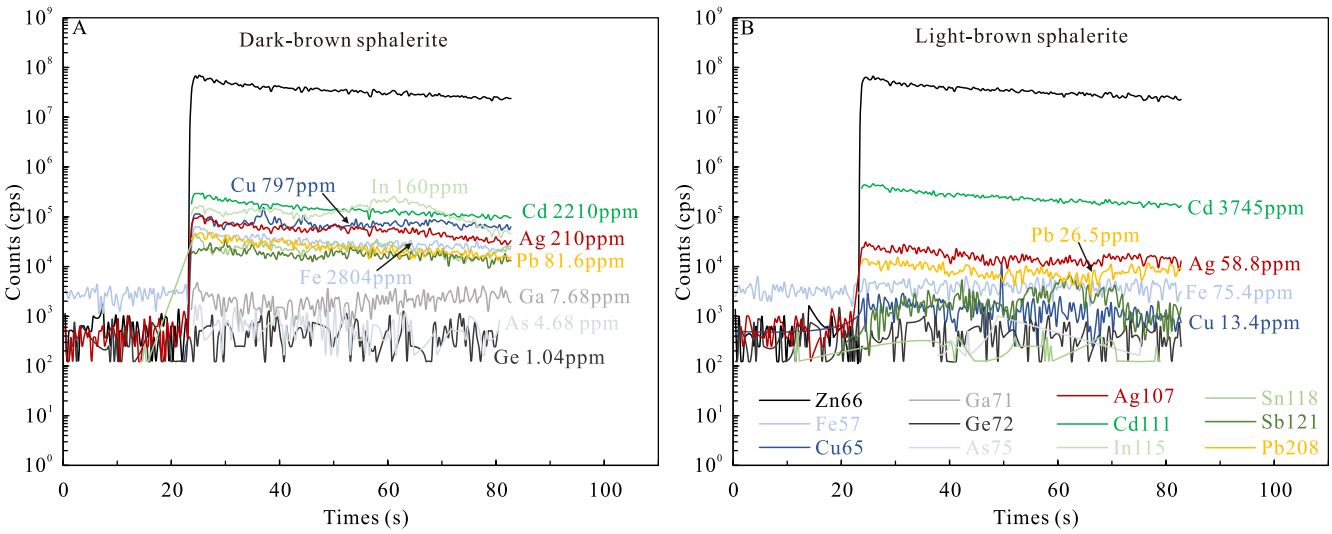

Fig. 9. Typical single-spot LA-ICP-MS spectra for selected elements of dark-brown sphalerite and light-brown sphalerite from the Shagou deposit.

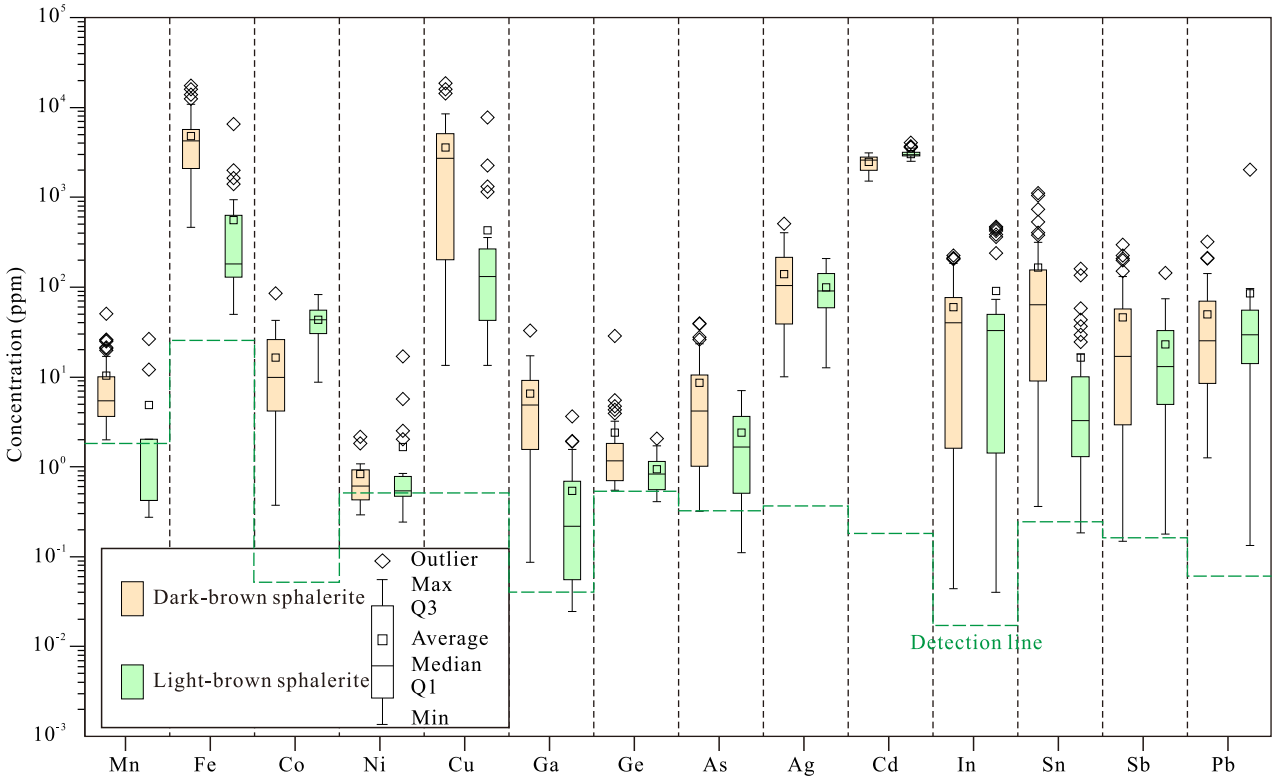

Fig. 10. Box-and-whisker plots of trace element compositions of dark-brown sphalerite and light-brown sphalerite from the Shagou deposit.

Seward, 2003). As the ore fluid cooled, the hydrothermal system gradually dropped in logfO_2 and logfS_2, which decreased the bisulfide solubility in the fluid, causing precipitation of silver mineral precipitation during the late stage. Thus, the reduction in temperature, logfO_2, and logfS_2 of the hydrothermal system were the key triggers for Ag precipitation.

6.3. Ore genesis

The genesis of Ag-Pb-Zn deposits in the Xiayu ore field remains controversial (Sui et al., 2000; Chen et al., 2004; Mao et al., 2006; Gao et al., 2011; Han et al., 2013, 2014; Li et al., 2013, Li et al., 2016). Geological characteristics, fluid inclusions, and C-O-S-Pb isotope features indicate that the Shagou ore veins are comparable to Ag-Pb-Zn veins hosted in clastic metasedimentary rocks (Beaudoin and Sangster, 1992; Han et al., 2013, 2014; Li et al., 2013), however, the newly obtained He-Ar-Pb isotopic evidence suggests that the sources of the Ag-Pb-Zn veins are closely related to contemporaneous magmatism, which is significantly different from the veins in to the surrounding rock (Beaudoin and Sangster, 1992). In addition, geochronological data and high-temperature and high-salinity fluid characteristics support the idea that the Shagou veins formed as part of magmatic–hydrothermal systems (Mao et al., 2006, 2010; Gao et al., 2011; Tian et al., 2023).

Several studies have demonstrated that the trace-element

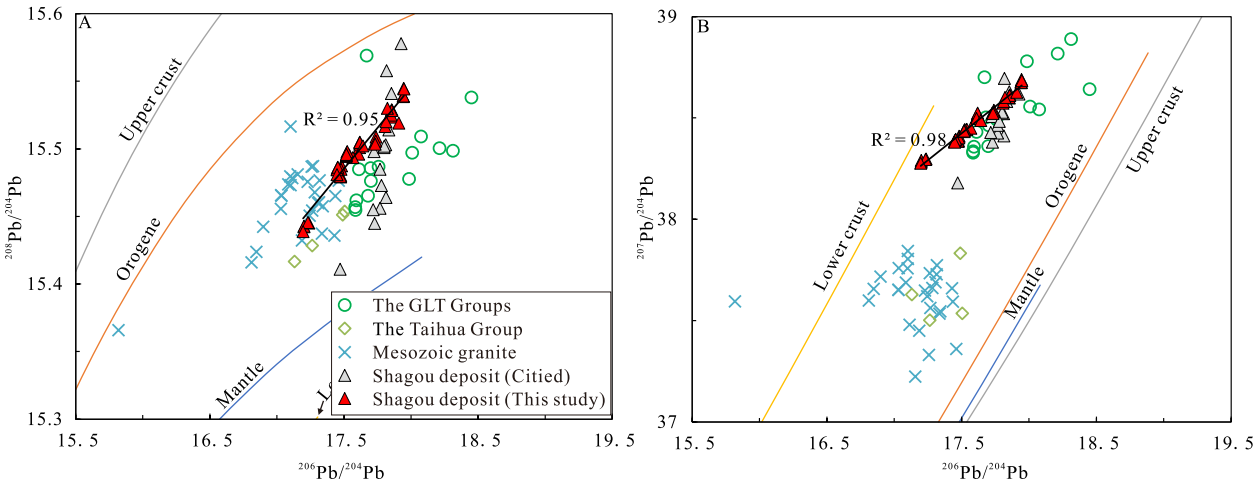

Fig. 11. Ag versus temperature diagram for dark-brown sphalerite and light-brown sphalerite from the Shagou deposit. Temperature was calculated using the formula suggested by Frenzel et al. (2016) (GGIMFis).

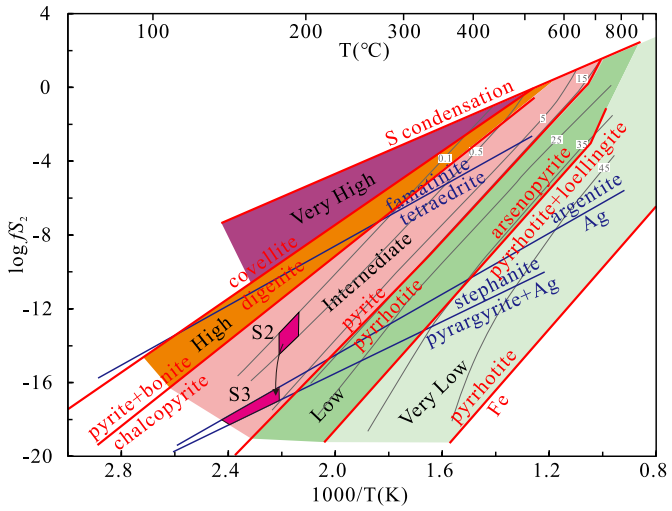

Fig. 12. logfS_2 versus temperature diagram showing the relative sulfidation state and the evolutionary path of hydrothermal fluids in the Shagou deposit. logfS_2 and temperature were calculated using the formulas suggested by Scott and Barnes (1971) and Frenzel et al. (2016) (GGIMFis), respectively. Sulfidation state determinations are from Einaudi et al. (2005).

composition of sphalerite can be related to the origin of a deposit (Cook et al., 2009; Ye et al., 2011; Frenzel et al., 2016; Bauer et al., 2019). Indium (In) is relatively enriched in magmatic-related deposits, whereas Ge and Cd are enriched in low-temperature hydrothermal systems. The dark-brown sphalerite of stage II is characterized by high In and low Ge concentrations from the Shagou deposit, consistent with sphalerite from a magmatic-related deposit (Fig. 13A). The light-brown stage III sphalerite is relatively enriched in Ge and depleted in In, indicating its relation to fluid evolution (Fig. 13B). However, the high In/Ge ratios of the light-brown sphalerite also support its magmatic affiliation (Fig. 13B). Therefore, these results, together with the newly obtained He-Ar-Pb isotopic data, suggest that the Shagou deposit is related to a magmatic-hydrothermal fluid system.

Many magmatic-hydrothermal Ag-Pb-Zn veins are closely related to porphyry Cu-Mo-Au deposits, i.e., veins in the Cordillera have a well-developed metal and alteration zonation from the center toward the margin (Fontboté and Bendezú, 2009; Bendezú and Fontboté, 2009; Kissin and Mango, 2014). Pb-Zn-Ag veins commonly occur in shallow, peripheral, and distal parts of a porphyry system, which provides a very useful guide for the exploration of newly discovered Ag-Pb-Zn veins near porphyry Cu-Mo-Au deposits and vice versa (Seedorff et al., 2005; Sillitoe, 2010; Wang et al., 2020, 2023; Deng et al., 2021; Hui et al., 2021).

Pb-Zn-Ag veins are widespread in the SNCC and have close temporal, spatial, and genetic associations with porphyry Mo mineralization in the Nannihu and Fudian ore fields (Cao et al., 2015; Li et al., 2017; Jin et al., 2019). However, such a relationship is lacking for Ag-Pb-Zn veins in the Xiayu ore field. The Xiayu ore field is characterized by Ag-Pb-Zn-Au-Cu-Mo polymetallic mineralization (Fig. 2; Chen et al., 2004; Mao et al., 2006; Deng et al., 2013; Li et al., 2016, 2017; Cao et al., 2017). These Ag-Pb-Zn deposits show obvious magmatic-hydrothermal affiliation (Mao et al., 2006; Gao et al., 2010, 2011; Li et al., 2016, this study). Monazite and xenotime U-Pb dating suggest that the Ag-Pb-Zn-Au-(Cu) veins were formed at 125.7 ± 1.8 Ma to 123.3 ± 1.7 Ma, which coincides with the age of the Haopinggou granite porphyry (P2; 125.9 ± 0.7 Ma; Tian et al., 2023). In addition, molybdenite-rich veins were found in the deep part of the Shagou deposit (Mao et al., 2006), and the copper content tended to increase in the depth of the Tieluping deposit (Wang, 2010). Therefore, we propose that unexposed porphyry Cu-Au-Mo deposits may exist beneath and/or to the side of some Pb-Zn-Ag veins, and the Xiayu ore field may be a potential exploration target for porphyry Cu-Au-Mo deposits.

7. Conclusions

(1) The He-Ar-Pb isotopes indicate that the ore-forming fluids and metals were mainly derived from a mixed source of Mesozoic granite, the surrounding Taihua Group and the Meso-Neoproterozoic marine sediments.

(2) Application of the sphalerite GGIMFis geothermometer yielded a mineralization temperature of 175 to 310 ℃ (mean ~224 ℃) and 143 to 240 ℃ (mean ~176 ℃) for the base metal and silver mineralization, respectively.

(3) The reduction in temperature, logfO_2, and logfS_2 of the ore-forming fluid were likely the key triggers for silver precipitation.

(4) The Shagou Ag-Pb-Zn veins are genetically related to a magmatic-hydrothermal fluid system.

Declaration of Competing Interest

The authors declare that they have no known competing financial interests or personal relationships that could have appeared to influence the work reported in this paper.

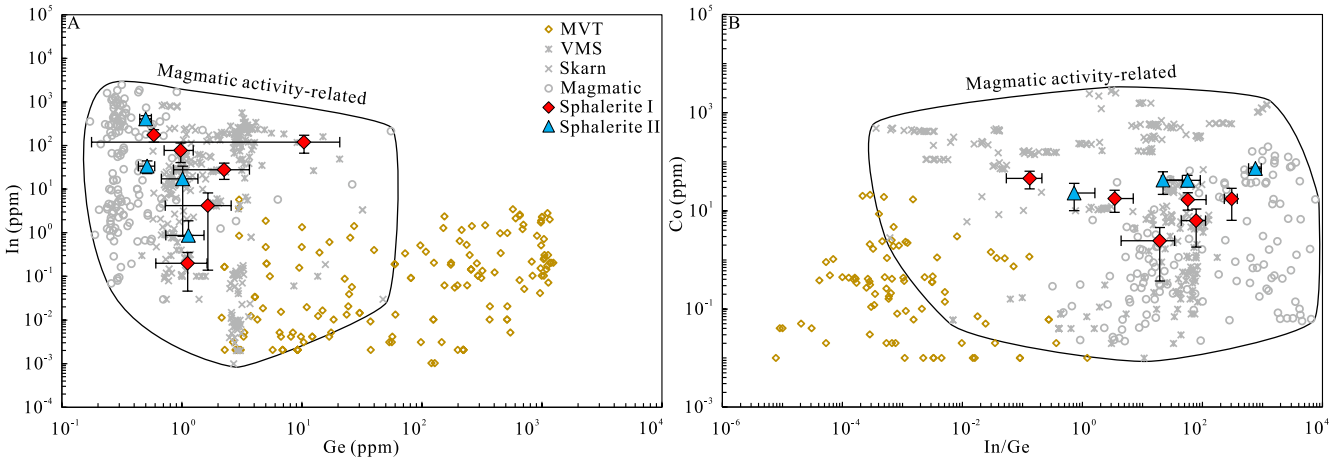

Fig. 13. In versus Ge (A), and Co versus In/Ge (B) diagram revealing the genetic type of the Shagou deposit. Data of MVT, VMS, skarn, and magmatic deposits were obtained from Cook et al. (2009), Ye et al. (2011), and Bauer et al. (2019).

Data availability

No data was used for the research described in the article.

Acknowledgements

The authors thank Mr. Shi Haisong and the staff of the Henan Found Mining Co., Ltd. for their assistance during fieldwork and Dr. Guohao Jiang (He-Ar isotope), Dr. Zhian Bao (Pb isotope), Dr. Zhihui Dai (trace element of sulfides), Dr. Xiang Li, and Wenqin Zheng (EPMA) for experimental analysis. This study was financially supported by the Research Fund for the Doctoral Program of Tongren University (No. trxyDH2016) and the Natural Science Foundation of China (NSFC Nos. U1812402, U1603245 and 41703051). This contribution forms part of the results of a cooperative project (Title: Geochemical model and deep prospecting prediction of silver polymetallic deposit, the Xiong'ershan district) between the Institute of Geochemistry, Chinese Academy of Sciences and Henan Province Non-ferrous Metals Geological Mineral Resources Bureau, which the authors participate in.

Appendix A. Supplementary data

Supplementary data to this article can be found online at https://doi.org/10.1016/j.oregeorev.2023.105765.

References

Bao, Z., Chen, L., Zong, C., Yuan, H., Chen, K., Dai, M., 2017. Development of pressed sulfide powder tablets for in situ sulfur and lead isotope measurement using LA-MC-ICP-MS. Int. J. Mass Spectrom. 421, 255–262.

Bauer, M.E., Burisch, M., Ostendorf, J., Krause, J., Frenzel, M., Seifert, T., Gutzmer, J., 2019. Trace element geochemistry of sphalerite in contrasting hydrothermal fluid systems of the Freiberg district, Germany: insights from LA-ICP-MS analysis, near-infrared light microthermometry of sphalerite-hosted fluid inclusions, and sulfur isotope geochemistry. Miner. Deposita 54 (2), 237–262.

Beaudoin, G., Sangster, D.F., 1992. A descriptive model for silver-lead-zinc veins in clastic metasedimentary terranes. Econ. Geol. 87 (4), 1005–1021.

Bendezú, R., Fontboté, L., 2009. Cordilleran epithermal Cu-Zn-Pb-(Au-Ag) mineralization in the Colquijirca district, central Peru: Deposit-scale mineralogical patterns. Econ. Geol. 104 (7), 905–944.

Bonsall, T.A., Spry, P.G., Voudouris, P.C., Tombros, S., Seymour, K.S., Melfos, V., 2011. The geochemistry of carbonate-replacement Pb-Zn-Ag mineralization in the Lavrion district, Attica, Greece: Fluid inclusion, stable isotope, and rare earth element studies. Econ. Geol. 106 (4), 619–651.

Burnard, P.G., Hu, R.Z., Turner, G., Bi, X.W., 1999. Mantle, crustal and atmospheric noble gases in Ailaoshan gold deposits, Yunnan Province, China. Geochim. Cosmochim. Acta 63 (10), 1595–1604.

Cao, M., Ya, J., Deng, X., Yang, F., Mao, G., Mathur, R., 2017. Diverse and multistage Mo, Au, Ag–Pb–Zn and Cu deposits in the Xiong'er Terrane, East Qinling: from Triassic Cu mineralization. Ore Geol. Rev. 81, 565–574.

Cao, H.W., Zhang, S.T., Santosh, M., Zheng, L., Tang, L., Li, D., Zhang, Y.H., 2015. The Luanchuan Mo-W-Pb-Zn-Ag magmatic-hydrothermal system in the East Qinling metallogenic belt, China: constrains on metallogenesis from C-H-O-S-Pb isotope compositions and Rb–Sr isochron ages. J. Asian Earth Sci. 111, 751–780.

Chen, Y.J., Fu, S.G., 1992. Gold Mineralization in west Henan, China. China Seismological Press, Beijing, pp. 1–234 in Chinese with English abstract.

Chen, Y.J., Pirajno, F., Sui, Y.H., 2004. Isotope geochemistry of the Tieluping silver-lead deposit, Henan, China: a case study of orogenic silver-dominated deposits and related tectonic setting. Miner. Deposita 39 (5), 560–575.

Cook, N.J., Ciobanu, C.L., Pring, A., Skinner, W., Shimizu, M., Danyushevsky, L., Melcher, F., 2009. Trace and minor elements in sphalerite: A LA-ICPMS study. Geochim. Cosmochim. Actam 73 (16), 4761–4791.

Deng, X.H., Chen, Y.J., Santosh, M., 2013. Metallogeny during continental outgrowth in the Columbia supercontinent Isotopic characterization of the Zhaiwa Mo-Cu system in the North China Craton. Ore Geol. Rev. 51, 43–56.

Deng, C., Li, C., Rong, Y., Chen, D., Zhou, T., Wang, X., Yin, R., 2021. Different metal sources in the evolution of an epithermal ore system: Evidence from mercury isotopes associated with the Erdaokan epithermal Ag-Pb-Zn deposit, NE China. Gondw. Res. 95, 1–9.

Dong, Y., Zhang, G., Neubauer, F., Liu, X., Genser, J., Hauzenberger, C., 2011. Tectonic evolution of the Qinling orogen, China: review and synthesis. J. Asian Earth Sci. 41 (3), 213–237.

Einaudi, M.T., Hedenquist, J.W., Inan, E.E., 2005. Sulfidation state of fluids in active and extinct hydrothermal systems: transitions from porphyry to epithermal environments. Soc. Econ. Geol. Special Publ. 10, 1–50.

Fontboté, L., Bendezú, R., 2009. Cordilleran or Butte-type veins and replacement bodies as a deposit class in porphyry systems. In Proceedings of the 10th Biennial Society of Geology Applied to Ore Deposits Meeting, pp. 521-523.

Frenzel, M., Hirsch, T., Gutzmer, J., 2016. Gallium, germanium, indium, and other trace and minor elements in sphalerite as a function of deposit type-A meta-analysis. Ore Geol. Rev. 76, 52–78.

Gammons, C.H., Barnes, H.L., 1989. The solubility of Ag_2S in near-neutral aqueous sulfide solutions at 25 to 300 °C. Geochim. Cosmochim. Acta 53 (2), 279–290.

Gao, J.J., Mao, J.W., Ye, H.S., Chen, M.H., Zheng, R.F., 2010. Geology and ore-forming fluid of silver-lead-zinc lode deposit of Shagou, western Henan Province. Acta Petrol. Sin. 26, 740–756 in Chinese with English abstract.

Gao, J.J., Mao, J.W., Chen, M.H., Ye, H.S., Zhang, J.J., Li, Y.F., 2011. Vein structure analysis and $^{40}Ar/^{39}Ar$ dating of sericite from sub-ore altered rocks in the Tieluping large-size Ag-Pb deposit of western Henan Province. Acta Geol. Sin. 85, 1172–1187 in Chinese with English abstract.

Gautheron, C., Moreira, M., 2002. Helium signature of the subcontinental lithospheric mantle. Earth Planet. Sci. Lett. 199 (1–2), 39–47.

Graham, D.W., 2002. Noble gas isotope geochemistry of mid-ocean ridge and ocean island basalts: characterization of mantle source reservoirs. Rev. Mineral. Geochem. 47, 247–317.

Guo, B., Zhu, L.M., Li, B., Gong, H.J., Wang, J.Q., 2009. Zircon U-Pb age and Hf isotope composition of the Huashan and Heyu granite plutons at the southern margin of North China craton: Implications for geodynamic setting. Acta Petrol. Sin. 25, 265–281 in Chinese with English abstract.

Han, J., Chen, H., Yao, J., Deng, X., 2015. 2.24 Ga mafic dykes from Taihua Complex, southern Trans-North China Orogen, and their tectonic implications. Precambr. Res. 270, 124–138.

Han, J.S., Yao, J.M., Deng, X.H., 2013. Sr-isotope constraint on the source of the fluids forming the Shagou Ag–Pb–Zn deposit, eastern Qinling orogen. Acta Petrol. Sin. 29, 18–26 in Chinese with English abstracts.

Han, J.S., Yao, J.M., Chen, H.Y., Deng, X.H., Ding, J.Y., 2014. Fluid inclusion and stable isotope study of the Shagou Ag–Pb–Zn deposit, Luoning, Henan province, China: implications for the genesis of an orogenic lode Ag–Pb–Zn system. Ore Geol. Rev. 62, 199–210.

Han, Y.G., Zhang, S.H., Pirajno, F., Wang, Y., Zhang, Y.H., 2009. New ^{40}Ar-^{39}Ar age constraints on the deformation along the Machaoying fault zone: Implications for Early Cambrian tectonism in the North China craton. Gondw. Res. 16, 255–263.
He, Y., Zhao, G., Sun, M., Xia, X., 2009. SHRIMP and LA-ICP-MS zircon geochronology of the Xiong'er volcanic rocks: implications for the Paleo-Mesoproterozoic evolution of the southern margin of the North China Craton. Precambr. Res. 168 (3–4), 213–222.
Hu, S.X., Lin, Q.L., Chen, Z.M., Li, S.M., 1988. Geology and Metallogeny of the Collision Belt Between the North and the South China Plates, Nanjing. Nanjing University Press, pp. 1–558 in Chinese with English abstract.
Hui, K., Qin, K., Li, Z., Wang, F., Gao, S., Han, R., Li, G., 2021. The linkage between the Jiawula-Chaganbulagen Ag-Pb-Zn and adjacent porphyry Mo-Cu mineralization, Inner Mongolia, northeast China. Ore Geol. Rev. 134, 104153.
Jin, C., Chen, W.T., Gao, X.Y., Li, X.C., Bao, Z.W., Zhao, T.P., 2019. Origin of the Wangpingxigou Pb-Zn deposit in East Qinling orogenic belt, China: Distal response to the giant Donggou porphyry Mo system? Ore Geol. Rev. 109, 101–116.
Kelley, K.D., Leach, D.L., Johnson, C.A., Clark, J.L., Fayek, M., Slack, J.F., Ridley, W.I., 2004. Textural, compositional, and sulfur isotope variations of sulfide minerals in the Red Dog Zn-Pb-Ag deposits, Brooks Range, Alaska: implications for ore formation. Econ. Geol. 99 (7), 1509–1532.
Kendrick, M.A., Burgess, R., Pattrick, R.A.D., Turner, G., 2001. Fluid inclusion noble gas and halogen evidence on the origin of Cu-porphyry mineralising fluids. Geochim. Cosmochim. Acta 65 (16), 2651–2668.
Kennedy, B.M., Hiyagon, H., Reynolds, J.H., 1991. Noble gases from Honduras geothermal sites. J. Volcanol. Geoth. Res. 45 (1–2), 29–39.
Kissin, S.A., Mango, H., 2014. Silver vein deposits. Treatise on geochemistry, second edition: Oxford, Elsevier, p. 425-432.
Lee, J.Y., Marti, K., Severinghaus, J.P., Kawamura, K., Yoo, H.S., Lee, J.B., Kim, J.S., 2006. A redetermination of the isotopic abundances of atmospheric Ar. Geochim. Cosmochim. Acta 70, 4507–4512.
Li, Y.F., 2005. The Temporal-Spatial Evolution of Mesozoic Granitoids in the Xiong'ershan Area and their Relationships to Molybdenum-Gold Mineralization. China University of Geosciences, pp. 1–135. Doctor's Thesis,(in Chinese with English abstracts.
Li, N., Chen, Y.J., McNaughton, N.J., Ling, X.X., Deng, X.H., Yao, J.M., Wu, Y.S., 2015. Formation and tectonic evolution of the khondalite series at the southern margin of the North China Craton: Geochronological constraints from a 1.85-Ga Mo deposit in the Xiong'ershan area. Precambr. Res. 269, 1–17.
Li, N., Chen, Y.J., Santosh, M., Pirajno, F., 2018. Late Mesozoic granitoids in the Qinling Orogen, Central China, and tectonic significance. Earth Sci. Rev. 182, 141–173.
Li, Z.K., Li, J.W., Zhao, X.F., Zhou, M.F., Selby, D., Bi, S.J., Zhao, Z.J., 2013. Crustal-extension Ag-Pb-Zn veins in the Xiong'ershan District, Southern North China craton: constraints from the Shagou deposit. Econ. Geol. 108 (7), 1703–1729.
Li, Z.K., Li, J.W., Cooke, D.R., Danyushevsky, L., Zhang, L., O'Brien, H., Xu, H.J., 2016. Textures, trace elements, and Pb isotopes of sulfides from the Haopinggou vein deposit, southern North China Craton: implications for discrete Au and Ag-Pb-Zn mineralization. Contrib. Mineral. Petrol. 171 (12), 171–199.
Li, Z.K., Bi, S.J., Li, J.W., Zhang, W., Cooke, D.R., Selby, D., 2017. Distal Pb-Zn-Ag veins associated with the world-class Donggou porphyry Mo deposit, southern North China craton. Ore Geol. Rev. 82, 232–251.
Li, H.M., Wang, D.H., Wang, X.X., Zhang, C.Q., Li, L.X., 2012. The Early Mesozoic syenogranite in Xiong'er Mountain area, southern margin of North China Craton: SHRIMP zircon U-Pb dating, geochemistry and its significance. Acta Petrol. Mineral. 31 (6), 771–782 in Chinese with English abstract.
Li, S.G., Xiao, Y.L., Liou, D.L., Chen, Y.Z., Wang, S.S., 1993. Collision of the North China and Yangtze Blocks and formation of coesite-bearing eclogites: timing and processes. Chem. Geol. 109 (1–4), 89–111.
Liang, T., Lu, R., Luo, Z.H., Bai, F.J., Liu, X., 2015. LA-ICP-MS U-Pb age of zircons from Haopinggou biotite granite porphyry in Xiong'er Moutain, Western Henan Province, and its geologic implications. Geol. Rev. 61, 901–912 in Chinese with English abstract.
Longerich, H.P., Jackson, S.E., Günther, D., 1996. Laser ablation inductively coupled plasma mass spectrometric transient signal data acquisition and analyte concentration calculation. J. Anal. At. Spectrom 11 (9), 899–904.
Mao, J.W., Zheng, R.F., Ye, H.S., Gao, J.J., Chen, W., 2006. ^{40}Ar/^{39}Ar dating of fuchsite and sericite from altered rocks close to ore veins in Shagou large-size Ag-Pb-Zn deposit of Xiong'ershan area, western Henan Province, and its significance. Mineral Deposits 25, 359–368 in Chinese with English abstract.
Mao, J.W., Xie, G.Q., Pirajno, F., Ye, H.S., Wang, Y.B., Li, Y.F., Zhao, H.J., 2010. Late Jurassic-Early Cretaceous granitoid magmatism in Eastern Qinling, central-eastern China: SHRIMP zircon U-Pb ages and tectonic implications. Aust. J. Earth Sci. 57 (1), 51–78.
Ni, Z.Y., Chen, Y.J., Li, N., 2012. Pb-Sr-Nd isotope constraints on the fluid source of the Dahu Au–Mo deposit in Qinling Orogen, central China, and implication for Triassic tectonic setting. Ore Geol. Rev. 46, 60–67.
O'Nions, R.K., Oxburgh, E.R., 1983. Heat and helium in the earth. Nature 306, 429–431.
Peng, E.S., 1994. Metallogenic characteristics of Haopinggou-Tieluping Silver-Gold polymetallic deposits. J. Central-South Instit. Min. Metallurgy 25 (4), 427–430 in Chinese with English abstract.
Qi, J.P., 2006. Geology, Geochemistry and Genesis of Vein Type Lead-Zinc-Silver Deposits in Luanchuan, Henan. Peking University, Beijing, pp. 1–114 in Chinese with English abstract.
Ren, J., Tamaki, K., Li, S., Zhang, J.X., 2002. Late Mesozoic and Cenozoic rifting and its dynamic setting in Eastern China and adjacent areas. Tectonophysics 344, 175–205.
Scott, S.D., Barnes, H.L., 1971. Sphalerite geothermometry and geobarometry. Econ. Geol. 66 (4), 653–669.
Seedorff, E., Dilles, J.H., Proffett, J.M., Einaudi, M.T., Zurcher, L., Stavast, W.J.A., Johnson, D.A., Barton, M.D., 2005. Porphyry deposits: Characteristics and origin of hypogene features. Econ. Geol. 100th Anniversary Volume, 251–298.
Seward, T.M., 1976. The stability of chloride complexes of silver in hydrothermal solutions up to 350 °C. Geochim. Cosmochim. Acta 40 (11), 1329–1341.
Shi, Q.Z., Wei, X.D., Li, M.L., Pang, J.Q., 2004. Nappe and Extensional Detachment Structures in North Side of east Qinling, Henan. Geological Publishing House, Beijing, pp. 1–204 in Chinese with English abstract.
Sillitoe, R.H., 2010. Porphyry copper systems. Econ. Geol. 105, 3–41.
Smith, H.A., Ross, A.A., Robinson, S., Webster, R., Chesher, R., Riles, A., 2020. Technical Report: NI 43-101 Technical Report Update on the Ying Ag-Pb-Zn Property in Henan Province, People's Republic of China. p. 1–274.
Stefansson, A., Seward, T.M., 2003. Experimental determination of the stability and stoichiometry of sulphide complexes of silver(I) in hydrothermal solutions to 400 °C at 500 bar. Geochim. Cosmochim. Acta 67, 1395–1413.
Stephenson, P.R., Fowler, A.P., Smith, H.A., 2016. Ying NI 43–101 Technical Report, Henan Province. China AMC Mining Consultants (Canada) Ltd, Vancouver, pp. 1–246.
Stoffregen, R.E., 1987. Genesis of acid-sulfate alteration and Au-Cu-Ag mineralization at Summitville, Colorado. Econ. Geol. 82, 1575–1591.
Stuart, F.M., Burnard, P.G., Taylor, R.E.A., Turner, G., 1995. Resolving mantle and crustal contributions to ancient hydrothermal fluids: He-Ar isotopes in fluid inclusions from Dae Hwa W Mo mineralization, South Korea. Geochim. Cosmochim. Acta 59 (22), 4663–4673.
Sui, Y.H., Wang, H.H., Gao, X.L., Chen, H.Y., Li, Z., 2000. Ore fluid of the Tieluping silver deposit of Henan Province and its illustration of the tectonic model for collisional petrogenesis, metallogenesis and fluidization. Sci. China Ser. D Earth Sci. 43, 108–121.
Tian, Y., Mao, J., Jian, W., Wang, Y., Feng, R., Ye, H., Wang, P., 2023. Recognition of the Xiayu intermediate-sulfidation epithermal Ag-Pb-Zn-Au (-Cu) mineralization in the East Qinling polymetallic ore belt: Constraints from Geology and Geochronology. Ore Geology Reviews, China, p. 105398.
Turner, G., Burnard, P., Ford, J., Gilmour, J.D., Lyon, I.C., Stuart, F.M., 1993. Tracing fluid sources and interactions. Philos. Trans. R. Soc. London. Series A: Phys. Eng. Sci. 344 (1670), 127–140.
Wang, F.G., 2010. Silver-gold deposit geochemical exploration model in Xiong'ershan region of western Henan. Mineral Resour. Geol. 24 (3), 256–262 in Chinese with English abstract.
Wang, Y., Cai, J., Liu, L., Zhou, J., Feng, P., Guo, Y., Guo, Y., 2023. A Permian intermediate-sulfidation epithermal Pb-Zn-Ag deposit in the northern margin of North China Craton. Ore Geol. Rev. 105492.
Wang, Z.G., Cui, H., Xu, M.L., 1997. The Tectonic Evolution and Mineralization in the South, Margin of North China Block. Metallurgical Industry Press, Beijing, pp. 1–254 in Chinese with English abstract.
Wang, C., He, X., Carranza, E.J.M., Cui, C., 2019. Paleoproterozoic volcanic rocks in the southern margin of the North China Craton, central China: implications for the Columbia supercontinent. Geosci. Front. 10 (4), 1543–1560.
Wang, X., Jiang, S., Dai, B.Z., 2010. Melting of enriched Archean subcontinental lithospheric mantle: Evidence from the ca. 1760Ma volcanic rocks of the Xiong'er Group, southern margin of the North China Craton. Precambr. Res. 182 (3), 204–216.
Wang, Y.T., Mao, J.W., Lu, X.X., 2001. ^{40}Ar-^{39}Ar dating and geochronological constraints on the ore-forming epoch of the Qiyugou gold deposit in Songxian county, Henan Province. Geol. Rev. 47, 551–555 in Chinese with English abstract.
Wang, Y., Zeng, Q., Liu, J., Wu, L., Qin, K., 2020. Porphyry Mo and epithermal Au-Ag-Pb-Zn mineralization in the Zhilingtou polymetallic deposit, South China. Miner. Deposita 55, 1385–1406.
Xu, J.H., Jiang, Y.P., Hu, S.L., Zhang, Z.W., Wu, C.Q., Zheng, C.F., Li, X.Y., Jin, Z.R., Zhang, S.S., Zhou, Y.T., 2021. Petrogenesis and post-collisional setting of the Paleoproterozoic A-type granites in the Xiong'ershan area along the southern margin of the North China Craton. J. Earth Sci. in press.
Ye, L., Cook, N.J., Ciobanu, C.L., Yuping, L., Qian, Z., Tiegeng, L., Danyushevskiy, L., 2011. Trace and minor elements in sphalerite from base metal deposits in South China: A LA-ICPMS study. Ore Geol. Rev. 39 (4), 188–217.
Zartman, R.E., Doe, B.R., 1981. Plumbotectonics-the model. Tectonophysics 75 (1–2), 135–162.
Zhai, D., Liu, J., Cook, N.J., Wang, X., Yang, Y., Zhang, A., Jiao, Y., 2018. Mineralogical, textural, sulfur and lead isotope constraints on the origin of Ag-Pb-Zn mineralization at Bianjiadayuan, Inner Mongolia, NE China. Mineralium Dep. 54 (1), 47–66.
Zhai, D., Williams-Jones, A.E., Liu, J., Selby, D., Voudouris, P.C., Tombros, S., Sun, H., 2020. The Genesis of the Giant Shuangjianzishan Epithermal Ag-Pb-Zn Deposit, Inner Mongolia, Northeastern China. Econ. Geol. 115 (1), 101–128.
Zhang, G.W., Bai, Y.B., Sun, Y., Guo, A.L., Zhou, D.W., Li, T.H., 1985. Composition and evolution of the Archaean crust in central Henan, China. Precambr. Res. 27, 7–35.
Zhang, Y.H., Zhang, S.H., Han, Y.G., Zhang, H.J., 2006. Strike-slip features of the Machaoying fault zone and its evolution in the Huaxiong terrane, southern North China Craton. J. Jilin Univ. (Earth Sci. Ed.) 36, 169–176 in Chinese with English abstract.
Zhang, T.Y., Zhu, J.W., 1996. The distinguishing model of remote sensing of shallow buried granite mass in eastern Qinling. Henan Geol. 14 (4), 287–291 in Chinese with English abstract.
Zhang, Z.W., Zhu, B.Q., Chang, X.Y., 2003. The geochemistry of the alkaline-rich intrusive rocks in east Qinling, central China. Earth Sci. Front. 10, 507–519 in Chinese with English abstract.

Zhao, T.P., Zhou, M.F., 2009. Geochemical constraints on the tectonic setting of Paleoproterozoic A-type granites in the southern margin of the North China Craton. J. Asian Earth Sci. 36, 183–195.
Zhao, T.P., Zhai, M.G., Xia, B., Li, H.M., Zhang, Y.X., Wan, Y.S., 2004. Study on the zircon SHRIMP ages of the Xiong'er Group volcanic rocks: constraint on the starting time of covering strata in the North China Craton. Chin. Sci. Bull. 9, 2495–2502.
Zheng, R.F., Mao, J.W., Gao, J.J., 2006. Characteristics of sulfide and silver minerals in Shagou silver-lead-zinc deposit of Xiong'er Shan, Henan Province, and their significance. Mineral Deposits 25, 715–726 in Chinese with English abstract.
Zhu, R.X., Yang, J.H., Wu, F.Y., 2012. Timing of destruction of the North China Craton. Lithos 149, 51–60.